TECHNISCHE UNIVERSITÄT WIEN

ATOMINSTITUT

DIPLOMARBEIT

Detection and quantification of entanglement in solid state physics: theory and experiment

zur Erlangung des akademischen Grades

Diplom-Ingenieurin

im Rahmen des Studiums

Masterstudium Technische Physik

eingereicht von

Julia Mathé
Matrikelnummer 11802442

ausgeführt am Atominstitut
der Fakultät für Physik der Technischen Universität Wien

Betreuung
Betreuer: Univ.-Ass. Dr. Nicolai Friis
Mitwirkung: Dr. Giuseppe Vitagliano

Wien, 23.10.2023

(Unterschrift Verfasser/in) (Unterschrift Betreuer/in)

Abstract

An open challenge in solid state physics is to understand the behaviour of strange metal systems governed by strong correlations. One way to probe and characterize this quantum critical behaviour is to use magnetic neutron scattering experiments together with tools from entanglement theory. This thesis investigates how the depth and range of entanglement may be verified and bounded by witnesses based on collective angular momentum observables. In particular, we focus on how to obtain the quantum Fisher information as a multipartite entanglement witness from neutron scattering data.

Statutory Declaration

I hereby declare that I have authored this project work report independently, that I have not used other than the designated sources/resources and that I have explicitly marked all sources which have been quoted as such either literally or by content.

Julia Mathé
Vienna, October 30, 2023

Acknowledgements

Most importantly, I would like to thank my supervisors Nicolai Friis and Giuseppe Vitagliano for giving me the opportunity to work on this thesis in their research group. I am very grateful for their support, kindness and patience.

In addition, I thank our collaborators Silke Bühler-Paschen and Federico Mazza at the Institute of Solid State Physics for their cooperation and for providing me with neutron scattering data. Lastly, I would like to thank Fakher Assaad and Sounak Biswas at the University of Würzburg for taking the time to discuss their simulations approach, as well as Mechthild Enderle, Ursula B. Hansen, and Paul Steffens at the ILL for sharing some of their expertise and insights regarding neutron scattering experiments with me.

Contents

1 Introduction

An open challenge in solid state physics is to understand systems that are governed by strong correlations. Some of these systems, such as strange metals, feature interesting topological phases. Neutron scattering experiments in combination with tools from entanglement theory provide one way to probe and characterize these systems' behaviour. Here, the notion of long-range entanglement and its verification is of special interest. This will become evident in the following review where we address some important concepts from condensed-matter physics, quantum information theory, and neutron scattering, and see how and to what extent these concepts may complement each other in the study of quantum correlations in solid state systems.

1.1 Why phases matter

The basic states of thermodynamic systems are typically described in terms of phases such as gas, liquid, and solid states of matter. Within a given phase, the physical properties of a system do not change. In order for the physics to change, a state must undergo a phase transition. Phases and phase transitions are often characterized as functions of external parameters such as temperature, pressure, or magnetic field. This is usually summarized graphically in one or many phase diagrams.

A remarkably successful and widely used framework that describes the thermodynamic and structural changes of materials undergoing phase transitions is known as Landau theory. Here, the idea is to explain phase transitions through some symmetry-breaking mechanism that is characterized by an order parameter. For this purpose, the free energy of a system is an important mathematical quantity describing the thermodynamics of a system. In Landau theory, the free energy is written as a functional that is an analytic function of the order parameter. The exact form of this functional depends on the symmetries of the system and type of phase transition under consideration. Phase transitions take place at points where the free energy is minimized. Landau theory is also useful in the study of critical phenomena that occur near such phase transition points.

Nowadays, there exists a more comprehensive framework than Landau theory, known as renormalization group and scaling theory. These methods are more widely applicable and involved than Landau theory due to their use of the concept of universality that describes how critical phenomena depend only on the dimension and symmetries of a system and not on its microscopic details.

Nevertheless, Landau theory remains very useful until today. One of the reasons for this is that the phases it describes can be probed with the help of linear response functions that can be obtained from experiments such as inelastic neutron scattering or magnetization measurements. However, it turns out that Landau theory cannot characterize all phases of matter because there exist distinct phases of the same symmetry, such as quantum Hall states. These phases are known as topological phases. They are characterized by non-local topological properties, are often robust against local perturbations, and phases may be classified using topological invariants. Topological phase transitions can be explained within the framework of renormalization group (RG) and scaling theory using methods based on effective field theories, scaling laws, (quantum) criticality studies, RG flow, or topological quantum field theories. Note that the application of such methods can be quite demanding, and that it requires some level of expertise to find and implement the right approach for a given topological phase being studied. A framework for both symmetry breaking and topologically ordered phases and phase transitions is presented in [1]. In particular, topological phases are characterized as patterns of entanglement, i.e. entanglement distributed among many different parties. In that sense, topologically ordered systems are said to be long-range entangled where long-range entanglement can be defined as non-convertibility to a product state under a special type of local transformation known as generalized stochastic local transformations [1]. Thus, topological phases are connected to the entanglement structure of the system. Consequently, it would be interesting to probe and distinguish between both symmetry-breaking and topologically ordered phases with the help of entanglement witnesses. In particular, topological ground states are often found to be

highly entangled, and it is possible to study how this entanglement changes with time and other physical parameters.

Solid state physicists find topological phases interesting mainly because they describe new quantum states of matter with unique properties that cannot be described within the traditional framework of Landau theory. These novel states may have unique properties. Due to their robustness against local perturbations and disorder, these phases show little susceptibility to impurities or imperfections, which is important for practical considerations. Some notable phases feature what is known as topologically protected edge or surface states, topological insulators, and superconductors.

For similar reasons, many solid state physicists study a special type of phase transition occurring at absolute zero temperature. This is known as a quantum critical (QC) point and leads to the emergence of a QC phase. These phases often exhibit universality and can be characterized in terms of scaling laws, i.e. physical observables diverge or show power-law behaviour near a QC point. Such phases are extensively studied because they often feature phenomena arising from strong correlations between particles, such as unconventional superconductivity or exotic magnetic phases. This is also very interesting from a quantum information point of view, as quantum correlations are generally related to the entanglement structure of the system. In [2], entanglement is viewed as a resource for a condensed matter system that makes it possible to characterize the change in its ground state wave function as the system approaches a QC point. Such considerations are useful when looking at condensed matter setups where the scaling behaviour may be used as a tool to evaluate entanglement and vice versa.

Now we know why it is worthwhile to study strongly correlated systems that can give rise to interesting phases, and that quantum information theory may provide a framework to study and characterize strong correlations in quantum many-body systems. Let us now introduce some important and relevant concepts from this framework.

1.2 General concepts from entanglement theory

To begin, let us introduce the notion of entanglement by considering a bipartite system. Bipartite means that there are two parties, traditionally referred to as Alice and Bob. Alice's subsystem is described by the Hilbert space $\mathscr{H}_A$, while Bob's subsystem is described by the Hilbert space $\mathscr{H}_B$. Together, the composite bipartite Hilbert space is written as a tensor product $\mathscr{H}_A \otimes \mathscr{H}_B$. Bipartite quantum states are then defined on $\mathscr{H}_A \otimes \mathscr{H}_B$. An *entangled state* of a bipartite system is defined as a state that cannot be written as a product. A state that can be written as such a product state is known as a *separable state*. In general, separable states are defined through convex combinations of pure product states. In many cases, one considers a system of two qubits, such as two spin-$\frac{1}{2}$ particles. A given spin state can then be defined in terms of the "up" $|\uparrow\rangle$ and "down" $|\downarrow\rangle$ eigenstates of the corresponding σ_z spin operator. The four possible product states of such a bipartite system are then given by $|\uparrow\rangle_A \otimes |\uparrow\rangle_B$, $|\downarrow\rangle_A \otimes |\downarrow\rangle_B$, $|\uparrow\rangle_A \otimes |\downarrow\rangle_B$, and $|\downarrow\rangle_A \otimes |\uparrow\rangle_B$. Such product states have well-defined measurement outcomes. For the state $|\uparrow\rangle_A \otimes |\downarrow\rangle_B$, this means that if Alice and Bob measure the spin of many particles in this state along the z-direction, Alice will always get the result "up", while Bob will always get the outcome "down".

Now it is also possible to consider linear combinations of these product states such as $\frac{1}{\sqrt{2}}(|\uparrow\rangle_A \otimes |\uparrow\rangle_B \pm |\downarrow\rangle_A \otimes |\downarrow\rangle_B)$ or $\frac{1}{\sqrt{2}}(|\uparrow\rangle_A \otimes |\downarrow\rangle_B \pm |\downarrow\rangle_A \otimes |\uparrow\rangle_B)$. These states are known as Bell states. Because they cannot be written as product states of their components, they are (maximally) entangled. If Alice and Bob measure the states in their respective bases, they cannot be sure which outcome they will get, since "up" and "down" now occur with equal probability. This means that no useful information about an individual system can be obtained from a single measurement outcome. However, if Alice and Bob communicated their seemingly random outcomes they would eventually notice that their measurements are correlated. If Alice measures "up" and the system is in either of the states $\frac{1}{\sqrt{2}}(|\uparrow\rangle_A \otimes |\uparrow\rangle_B \pm |\downarrow\rangle_A \otimes |\downarrow\rangle_B)$, Bob must find his qubit to be in the same position. On the other hand, Bob's qubit would be pointing in the opposite direction in the case of either

of the states $\frac{1}{\sqrt{2}}(|\uparrow\rangle_A \otimes |\downarrow\rangle_B \pm |\downarrow\rangle_A \otimes |\uparrow\rangle_B)$. Note that if both Alice and Bob change their measurement basis to $|\pm\rangle = \frac{1}{\sqrt{2}}(|0\rangle \pm |1\rangle)$, and rewrite their states accordingly, they will similarly be able to distinguish between symmetrized and anti-symmetrized states.

So far, we have mainly considered *pure states*, i.e. states that can describe the system using only a single ket vector $|\Psi\rangle$. This is different from a *mixed state* that can be written as a statistical ensemble of pure states. This is usually written in terms of density matrices $\rho = \sum_m p_m |\Psi_m\rangle \langle\Psi_m|$. As an example, the Bell state $|\Psi^+\rangle = \frac{1}{\sqrt{2}}(|\uparrow\rangle_A \otimes |\uparrow\rangle_B + |\downarrow\rangle_A \otimes |\downarrow\rangle_B)$ is a pure state. The reduced states, $\rho_A = \mathrm{Tr}_B(\rho_{AB})$ and $\rho_B = \mathrm{Tr}_A(\rho_{AB})$, however, are mixed states. Thus, a state is entangled if it is pure and its subsystems are in a mixed state. In Schrödinger's formulation, one would say that "the system as a whole has less uncertainty than its parts."

Note that a mixed state may have many decompositions, of which some can be entangled even if the state itself is separable. Thus, a state is separable if there exists at least one decomposition in which it is a convex combination of pure product states.

In solid state physics, one often considers a lattice of N nodes, where each node represents a d-level quantum system. This means that we are also considering a Hilbert space of N d-level systems. The density matrix describing such a system is fully separable if there exists at least one decomposition (among the infinitely many) that is of the form

$$\rho_{\mathrm{sep}} = \sum_i p_i (\rho_1 \otimes \cdots \otimes \rho_N)_i \tag{1}$$

with $p_i \geq 0, \sum_i p_i = 1$. Otherwise, it is called entangled.

The structure of entanglement can be further characterized using the concepts of depth and range of entanglement. For these purposes, let us first introduce the notion of k-producibility. A state is k-producible if it can be written as

$$\rho_{k-\text{prod}} = \sum_i p_i (\rho_{S_1} \otimes \cdots \otimes \rho_{S_M})_i \tag{2}$$

with $p_i \geq 0, \sum_i p_i = 1$, and with ρ_{S_i} describing a partition of the Hilbert space into a subsystem containing at most k d-level systems. If a state is not k-producible, it has a *depth of entanglement* of $(k+1)$.

As an example, consider the two-particle system described above. The four product states are separable and have a depth of entanglement $k = 1$. The four Bell states, however, are maximally entangled with $k = N = 2$.

As indicated by the name, the range or width of entanglement contains information about the spatial structure of entanglement. Thus, the range of entanglement is always defined based on the spatial arrangement of the N d-level systems. In solid state physics, atoms are usually arranged on a lattice, such as a triangular, square, or hexagonal lattice where the number of neighbours of each atom as well as the spacing between the atoms are assumed to be constant. For a pure state, the *range of entanglement* is defined as the maximum distance of two entangled particles within the states $w(|\Psi\rangle)$.

Hence, the system is required to be arranged in space in a way that allows the characterization of such a distance, such as a string or lattice of any geometry, as is shown in Fig. 1.

For a general mixed state, the range of entanglement is defined as the minimum distance out of all maximum distances between two entangled particles over all (infinitely many) pure state decompositions [3]

$$w(\rho) = \min_{\mathscr{D}(\rho)} w(|\Psi_i\rangle \langle\Psi_i|) \tag{3}$$

where $\mathscr{D}(\rho)$ is the set of all decompositions $\{(p_i, |\Psi_i\rangle)\}_i$ for which $\rho = \sum_i p_i |\Psi_i\rangle \langle\Psi_i|$ with $0 \leq p_i \leq 1$ and $\sum_i p_i = 1$.

Note how the depth of entanglement provides a lower bound to the range.

Further efforts to characterize the structure of entanglement have been made, in particular in [4], where the depth of entanglement k and the h-inseparability, i.e. into how many subsets a system can be divided, are characterized with the help of Young diagrams, as can be seen in Fig. 1. Separately, k and h contain only very limited information about the structure of entanglement in the entire system, since k only considers the largest entangled subset, and h does not contain any information about the size of the entangled subsets. To combine the information present in k and h, Dyson's rank $r = k - h$ can be introduced and related to observable quantities such as the quantum Fisher information that will be of great relevance in the following chapters [4].

1.3 Entanglement verification and quantification

In general, it is a hard problem to determine whether a state is entangled, i.e. whether among the infinitely many pure-state decompositions there exists any decomposition of a given state into separable states.

First, let us introduce a fundamental tool in entanglement theory known as the Schmidt decomposition. For a general bipartite system in $\mathscr{H}_A \otimes \mathscr{H}_B$, the Schmidt decomposition can be written as

$$|\Psi\rangle_{AB} = \sum_k \lambda_k |k_A\rangle |k_B\rangle , \tag{4}$$

where $|k_A\rangle$ and $|k_B\rangle$ are orthonormal states for the systems A and B, respectively, and the $\lambda_k \geq 0$ are the Schmidt coefficients, for which $\sum_k \lambda_k^2 = 1$.

Many important entanglement quantifiers are based on the states' squared Schmidt coefficients λ_k^2, and their number which is known as the Schmidt rank $r_S(\Psi)$. One way to define the Schmidt number for mixed states is to maximize over all states within a given decompositions and then take the minimum over all such decompositions, i.e. [5]

$$r_S(\rho) = \inf_{\mathscr{D}(\rho)} \left(\max_{|\Psi_i\rangle \in \{(p_i, |\Psi_i\rangle)\}_i} \mathrm{r}(|\Psi_i\rangle \langle\Psi_i|) \right). \tag{5}$$

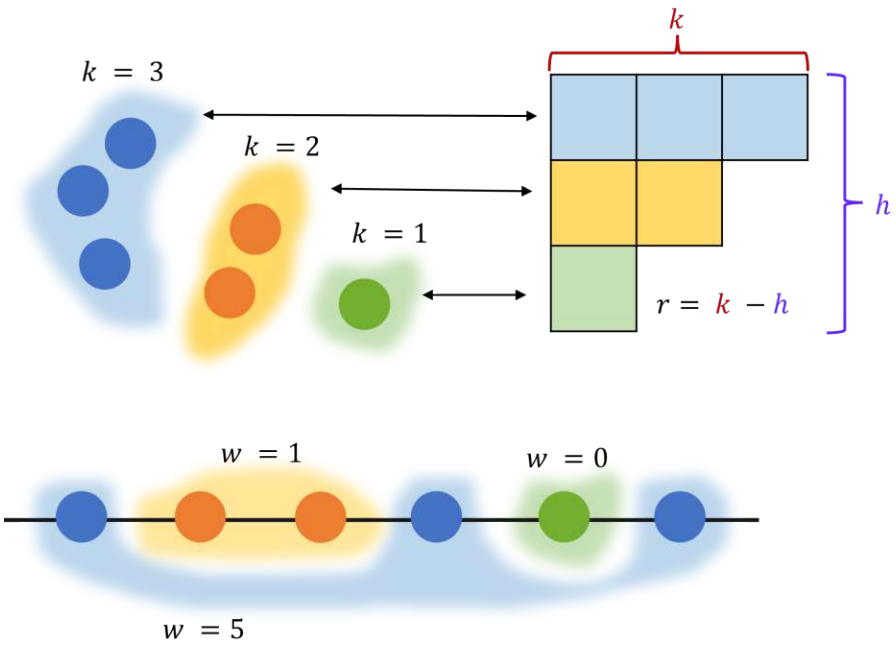

Figure 1: Describing the structure of entanglement with the help of the range of entanglement [3] and a Young diagram [4]. The top part of the figure shows how the entanglement structure of a system of $N = 6$ particles can be described in terms of its entanglement depth $k = 3$ and its separability into $h = 3$ subsystems. Combining this information, we can obtain Dyson's rank r, and draw the Young diagram; the width and height of the diagram correspond to k and h, respectively. The bottom part of the figure depicts the range of entanglement w for the system corresponding to a string of N particles situated at equal distance.

For pure states, the Schmidt number is equal to the Schmidt rank, and for separable states the Schmidt number is equal to 1.

A prominent example based on the Schmidt decomposition is the entanglement entropy as the Shannon entropy of the squared Schmidt coefficients. While these measures have a very straightforward interpretation and can be generalized for mixed states, they are not very practical for large systems due to the sheer size and exponential scaling of the systems under consideration, especially in the case of multipartite entanglement.

In fact, it is only possible to lower-bound the amount of entanglement present in any given system. This may generally be achieved by means of entanglement monotones that are non-increasing under local operations and classical communication (LOCC). One way this can be realized in the bipartite system $A \cup B$ would be to perform a local operation on the subsystem A, and then classically communicate the result to subsystem B, e.g. Alice calls Bob on the phone and tells him about her outcome. Based on this new information, Bob may then perform another local operation on his subsystem.

In practice, entanglement witnesses [6] are most commonly used to verify and quantify the entanglement present in a system. Consider the space of all separable states $\mathfrak{S}$ that is a convex subset of all quantum states $\mathfrak{Q}$ (i.e. separable and entangled states). By the Hahn-Banach theorem, there exists an *entanglement witness* (EW) for every entangled state characterized by an observable W, i.e. a hyperplane that separates the state from $\mathfrak{S}$ such that $\langle W \rangle = \mathrm{Tr}(W\rho) \geq 0 \quad \forall \rho \in \mathfrak{S}$, see Fig. 2. Thus, a given state ρ is entangled if $\mathrm{Tr}(W\rho) < 0$. For each entangled state, there exists a witness that detects it, as was proven in [7]. Note that W is not a separability witness, i.e. finding $\mathrm{Tr}(W\rho) \geq 0$ does not imply that the state is separable but that it is part of the subset of states that are not detected as entangled by the witness under consideration. For general systems, there exists a plethora of EWs as functionals of the system's density matrices designed to probe a subspace characterized by some specific entanglement structure. In practice, EWs can easily be constructed from experimentally measurable quantities such as the expectation values of spin operators, as we will see in the following sections.

1.3.1 In solid state physics

Ideally, measures for entanglement verification and characterization can be simulated numerically and probed experimentally. Consequently, in most experiments and theoretical models designed to probe entanglement, entanglement measures are applied to very specific and/or well-controlled systems where the number of particles is known, or can be estimated with some uncertainty. There are setups in which the individual parties can be directly

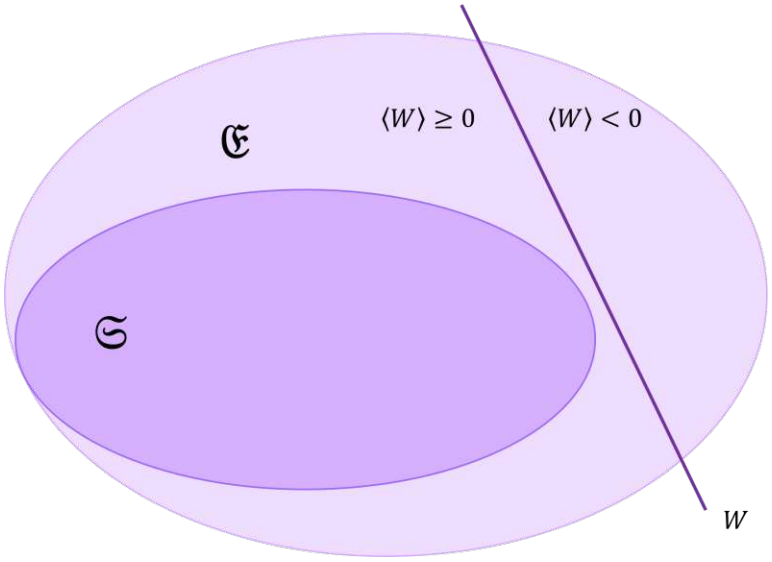

Figure 2: The idea of an entanglement witness. $\mathfrak{S}$ denotes the set of all separable states, and $\mathfrak{E}$ the set of all entangled states. The dark purple line represents the entanglement witness that separates the set of all states in such a way that for any state ρ on the right-hand side of the line, the expectation value $\langle W \rangle = \mathrm{Tr}(W\rho) < 0$. Hence, ρ is entangled. For any state ρ' on the left-hand side of the line, we have that $\langle W \rangle = \mathrm{Tr}(W\rho') \geq 0$. This means that this witness cannot determine whether ρ' is entangled or not.

probed, e.g. in some photonic systems. When working with pure states, one can look at specific subspaces of the system's Hilbert space, and at entanglement measures that are directly derived from the reduced density matrices, such as the entanglement entropy for bipartite entanglement. In other setups, such as cold atom systems, however, local parties cannot be probed and only global measurements are possible.

Strange metals and strongly correlated electron systems, however, are very different from these almost ideal systems in that they are complex many-body systems that are usually challenging to understand theoretically and model numerically. Also, in macroscopic systems we can usually only probe bulk and surface properties instead of individually addressing few-party

subspaces. Consequently, it is important to understand that there exists a big discrepancy between what is theoretically understood and possible and what is experimentally reasonable, and that an important challenge is to find general, non-trivial measures that are feasible to implement. Some efforts have been made in this direction, such as in [8–10] for neutron scattering experiments, where they tested measures based on tangles, the concurrence, and the quantum Fisher information. Since all of them have been experimentally implemented for a spin-$\frac{1}{2}$ quasi-Heisenberg antiferromagnet, they may provide a good starting point for probing entanglement in magnetic systems.

For a system of three qubits, the tangle [11] was introduced as a means to characterize how the entanglement between two qubits restricts the entanglement between the third qubit and each of the two qubits. It is related to a quantity known as entanglement of formation, which measures the entanglement entropy of a bipartite system and can be generalized to mixed bipartite states. In particular, the one-tangle characterizes the entanglement of a subsystem with its complement. It has a straightforward implementation for pure states in the XY model, i.e. $\tau_1 = \frac{1}{4} - \langle S_j^z \rangle$ for the entanglement of the site j with the remaining system [12]. For mixed states, one must consider the minimum average of $\langle S_j^z \rangle$ evaluated on all possible decompositions of the density matrix [12]. An experimentally accessible expression in terms of the magnetization can then be found by introducing $M^z = \langle S^z \rangle = \langle \sum_j s_z^{(j)} \rangle$. Since the one-tangle is based on the entanglement of a single pure state with its complement system, it is only defined at $T = 0$ K. However, at low temperatures one may expect the measure to hold within $k_B T$ relative to the energy of the elastic line at zero energy transfer [8], where it may be written in terms of the structure factor as $t_1 \approx 1 - 4 \sum_{\alpha,\beta=x,y,z} \int_{-k_B T}^{k_B T} d\omega \int_{B.Z} d\vec{q} \mathcal{S}^{\alpha\beta}(\vec{q}, \omega)$. For long-range entanglement, one would consequently expect a large value of t_1 within the appropriate temperature regime. Unfortunately, the one-tangle is a very involved concept and difficult to compute, as it cannot generally be expressed in terms of the magnetization. [8] makes use of a special case that is of very limited practical relevance.

The concurrence was originally defined as an entanglement monotone quantifying entanglement in a system of two qubits [13, 14] and was subsequently generalized to multi-particle states [15, 16] in arbitrary dimensions with extensions to continuous-variables in infinite dimensions [17]. To illustrate, for a bipartite pure state in $\mathcal{H}_{AB} = \mathcal{H}_A \otimes \mathcal{H}_B$ the concurrence can be written as $C(|\Psi\rangle) = \sqrt{2(1 - \mathrm{Tr}(\rho_A))}$. This expression can be generalized to n-partite systems by minimizing over the set of all possible bi-partitions [18], and to mixed states by taking the convex roof $C(\rho) = \inf_{p_i, |\Psi_i\rangle} \sum_i p_i C(|\Psi_i\rangle)$. In this form, the concurrence is very hard to compute and measure experimentally. Similar to the one-tangle, there exist some experimentally relevant generalizations for pairs of spins in a spin-$\frac{1}{2}$-system separated by some distance r that can be probed through the measurement of the two-tangle[8] $\tau_2 = 2\sum_{r\neq 0} C_r^2$ by spin-spin correlations and magnetization measurements. However, for highly correlated systems that cannot be easily modelled by a simplified version of the Heisenberg Hamiltonian, it may not be possible to find similar generalizations of the one-tangle or the concurrence that can still be calculated.

In [8–10], it was found that the quantum Fisher information shows promising results, which will be of particular interest to us since it can be obtained from neutron scattering observables and is applicable to general multipartite systems of arbitrary spin. In what follows, we will see that the quantum Fisher information can be viewed as a special case of measures based on collective variances and has a "complementary" measure in terms of the global variance of a given observable.

Recently, the work on the quantum Fisher information has been generalized and complemented in [19] where the authors investigate the spatial structure of quantum correlations compared to classical correlations in a system of weakly coupled spin-$\frac{1}{2}$ Heisenberg chains. To characterize this spatial dependence, the quantum coherence length is introduced and found to be finite at finite temperatures, irrespective of the magnetic order correlations.

Further difficulties arise in interesting systems that we do not know how to describe well theoretically. Such difficulties will become quite apparent in

this project, where the experimental interest is to consider strange metal systems in a QC state. For such a "black box" state, it is already difficult to make any statement about entanglement at all, as will become clear in the following chapters.

A more exhaustive review of entanglement in condensed matter systems is given in [20]. In particular, the authors show important results for the entanglement of pure states present in a system that is partitioned in real space into two areas A and B. Analyzing the eigenvalues of the reduced density matrix of a subsystem is referred to as entanglement spectroscopy, while the computation of the von Neumann entropy from the reduced density matrix is known as the entanglement entropy. The latter leads to the emergence of the area law, which tells us that the entanglement present in a subsystem often grows like the area of its boundary (and not like its volume). Corrections of the area law can be used to characterize the order of physical systems.

To summarize, it is interesting to investigate whether and to what extent the experimentally accessible observables used to characterize these systems can be used to understand the entanglement properties of these materials. Vice versa, one may ask what the entanglement structure of the quantum correlations present in the system may teach us about the physical observables and phases of the system. In what follows, we will investigate how to construct entanglement witnesses for solid state systems.

1.4 Neutron scattering fundamentals

Neutron scattering is a useful technique to probe the dynamics of a system since neutrons do not interact much with the sample compared to other (charged) probes. In general, there are two interaction mechanisms: the strong interaction between the neutrons and the atomic nuclei that leads to nuclear scattering, and the electromagnetic interaction between the neutrons' magnetic moments and the sample's magnetic structure that gives rise to magnetic scattering. The strength of these interactions can be characterized by the nuclear and magnetic interaction potentials, the subsequent expressions are often referred to as scattering length operators [21]. We focus on

unpolarized neutron scattering and want to measure the double differential cross-section, which can be written as the sum of both contributions:

$$\left(\frac{d^2\sigma}{d\Omega dE}\right) = \left(\frac{d^2\sigma}{d\Omega dE}\right)_{\text{nuclear}} + \left(\frac{d^2\sigma}{d\Omega dE}\right)_{\text{magnetic}}. \tag{6}$$

Both terms can be further decomposed as the sum of their coherent and incoherent contributions. The incoherent contribution is proportional to the variance in the scattering length and results from the behaviour of individual particles. The coherent contribution is proportional to the average of the scattering length and contains information about the structure of the material and collective behaviour such as the nuclear and magnetic Bragg peaks.

In addition, each term can be written as the sum of their elastic, quasi-elastic and inelastic contributions. Elastic scattering occurs at $\omega = 0$, i.e. where there is no energy exchange between the incoming neutron and the sample. Inelastic scattering allows us to probe excitations that interact with the incoming neutron, such as phonons, and yields peaks centered at specific energies. Quasi-elastic scattering results from diffusive dynamics and leads to a broadening of the elastic peak. In the following data analysis, we performed our measurements in the absence of Bragg peaks, and will focus on distinguishing between contributions from incoherent elastic scattering and quasi-elastic scattering.

1.4.1 Magnetic neutron scattering

Since we are dealing with magnetic materials, we will be interested in the magnetic scattering cross section that we will derive from the total scattering cross section written as [22]

$$\frac{d^2\sigma}{d\Omega dE_f} = \frac{k_f}{k_i}\left(\frac{m_n}{2\pi\hbar^2}\right)^2 \sum_{\lambda_i} p_{\lambda_i} \sum_{\lambda_f} |\left\langle \sigma_f \lambda_f \right| V(\vec{q}) \left| \sigma_i \lambda_i \right\rangle|^2 \delta(E_{\lambda_f} - E_{\lambda_i} - \hbar\omega), \tag{7}$$

where k_f and k_i are the final and initial neutron wave vector, respectively, and m_n is the mass of the neutron. The sum is taken over all possible initial

and final states of the neutron and sample, with σ_i and σ_f describing the initial and final neutron spin states, and λ_i and λ_f summarising the quantum numbers of the sample's initial and final state. The E_{λ_i} and E_{λ_f} denote the initial and final neutron energy, and $V(\vec{q})$ is the interaction potential that depends on the momentum transfer $\vec{q}$ that is also known as the scattering vector.

Note that the interaction potential contains both a magnetic and a nuclear contribution, $V(\vec{q}) = V_N(\vec{q}) + V_M(\vec{q})$. Since this expression is squared, one must in principle account for and distinguish between magnetic, nuclear, and nuclear-magnetic interference scattering. For unpolarized neutrons, the interference term vanishes. Another useful simplification comes from the fact that magnetic form factors generally decrease with an increase in q, whereas nuclear form factors show an increase with q^2 [22], allowing for the separation of nuclear and magnetic contributions in many cases. In this project, we are dealing with cerium compounds. In [23], the magnetic form factor of Ce has been investigated in great detail, and it was found that the form factor is generally dominated by the 4f contribution, and highly sensitive to the crystal field.

The magnetic contribution then corresponds to [22]

$$V_M(\vec{q}) = -2\gamma\mu_N \vec{s}_n \cdot M_\perp(\vec{q}),$$

where γ is the gyromagnetic ratio, μ_N is the nuclear magneton, $\vec{s}_n$ is the spin of the neutron, and $M_\perp(\vec{q})$ is the magnetic interaction vector, i.e. the component of the magnetization perpendicular to $\vec{q}$. This leads to a magnetic response function of

$$\mathcal{S}(\vec{q},\omega) = \sum_{\lambda_i} p_{\lambda_i} \sum_{\lambda_f} |2 \left\langle \sigma_f \right| \vec{s}_n \left| \sigma_i \right\rangle \cdot \left\langle \lambda_f \right| M_\perp(\vec{q}) \left| \lambda_i \right\rangle|^2 \delta(E_{\lambda_f} - E_{\lambda_i} - \hbar\omega).$$

Working with unpolarized neutrons, this expression can be written as [22, 24]

$$\mathcal{S}(\vec{q},\omega) = \sum_{\lambda_i} p_{\lambda_i} \sum_{\lambda_f} |\langle\lambda_i| M_\perp(\vec{q}) |\lambda_i\rangle|^2 \delta(E_{\lambda_f} - E_{\lambda_i} - \hbar\omega)$$
$$= \sum_{\alpha\beta} (\delta_{\alpha\beta} - \hat{q}_\alpha \hat{q}_\beta) S_{\alpha\beta}(\vec{q},\omega), \tag{8}$$

with $\alpha \in \{x, y, z\}$, and

$$S_{\alpha\beta}(\vec{q},\omega) = \frac{1}{2\pi\hbar} \int_{-\infty}^{\infty} dt \langle M_\alpha^\dagger(\vec{q}) M_\beta(\vec{q},t)\rangle e^{-i\omega t}$$
$$= \frac{N}{2\pi\hbar} \int_{-\infty}^{\infty} dt \int d^3r \Gamma_{\alpha\beta}(\vec{r},t) e^{-i(\vec{q}\vec{r}-\omega t)}. \tag{9}$$

$\Gamma_{\alpha\beta}(\vec{r},t) = \frac{1}{N} \int d^3r' \langle M_\alpha^\dagger(\vec{r}',0) M_\beta(\vec{r}'+\vec{r},t)\rangle$ is defined as the magnetic pair-correlation function.

If one makes the assumption that the magnetic moments are localized, and that scattering does not lead to a change in the atomic motion, it is possible to write this expression as [22]

$$S_{\alpha\beta}(\vec{q},\omega) = \frac{1}{2\pi\hbar} \sum_{jk} e^{-W_j - W_k} e^{\vec{q}(\vec{r}_k - \vec{r}_j)} \cdot \int_{-\infty}^{\infty} dt \langle M_{\alpha j}^\dagger(\vec{q}) M_{\beta k}(\vec{q},t)\rangle e^{-i\omega t}. \tag{10}$$

Now it is also possible to divide the magnetic response function into an elastic part, i.e. magnetic Bragg peaks, and a non-elastic part, [22, 24]

$$S_{\alpha,\beta}(q,\omega) = \langle M_\alpha(q)\rangle\langle M_\beta(-q)\rangle\delta(\hbar\omega) + \int_{-\infty}^{\infty} e^{-i\omega t} \langle \Delta M_\alpha(q) \Delta M_\beta(-q,t)\rangle \frac{dt}{2\pi\hbar}. \tag{11}$$

The dynamic part is then written as

$$\tilde{S}_{\alpha,\beta}(q,\omega) = \int_{-\infty}^{\infty} e^{-i\omega t} \langle \Delta M_\alpha(q) \Delta M_\beta(-q,t)\rangle \frac{dt}{2\pi\hbar}. \tag{12}$$

This expression is often referred to as the *dynamic (magnetic) structure factor*. The entire expression is often considered as the dynamic structure

factor. However, for our purposes it is only the non-elastic part that is to be considered; the first term merely accounts for the static order of the magnetic moments and contains no information about the dynamics of the system.

The dynamic structure factor further obeys several sum rules, as well as the detailed-balance constraint and the fluctuation-dissipation theorem (FDT). The most important relations are those that relate the cross section [22]

$$\frac{d\sigma}{d\Omega dE_f} = \frac{k_f}{k_i}\left(\frac{\gamma r_0}{2\mu_B}\right)^2 \mathcal{S}(\vec{q},\omega) \tag{13}$$

to $\mathcal{S}(\vec{q},\omega) = \sum_{\alpha\beta}(\delta_{\alpha\beta} - \hat{q}_\alpha\hat{q}_\beta)S_{\alpha\beta}(\vec{q},\omega)$ for unpolarized neutrons where

$$S_{\alpha\beta}(\vec{q},\omega) = \frac{1}{2\pi\hbar}\int_{-\infty}^{\infty} dt \langle M_\alpha^\dagger(\vec{q}) M_\beta(\vec{q},t)\rangle e^{-i\omega t}, \tag{14}$$

whose dynamical part can be related to the imaginary part of the generalized susceptibility by the FDT [22]

$$\tilde{S}_{\alpha\beta}(\vec{q},\omega) = (1+n(\omega))\frac{1}{\pi}\chi''_{\alpha\beta}(\vec{q},\omega), \tag{15}$$

where $n(\omega)$ is the Bose-Einstein distribution.

This is a useful result, as will become evident in the following sections. It is also important to note that these particular sum rules should be applied to scattering cross sections obtained in absolute units. This is not usually the case, as normalized data is not required in most experiments.

Dipole approximation

The idea of the dipole approximation [22] is to assume that the directions of spin and orbital magnetization within the atom are fixed, and that the magnetization is isotropically distributed. This applies well if q is smaller than the reciprocal of the atomic radius, and may still yield reasonable results for larger q. Note that the approximation neglects contributions from filled

shells and assumes atomic-like orbitals for unpaired electrons. As a general result of the dipole approximation we have [22]

$$M(\vec{q}) \cong -2\mu_B\big[\langle j_0(q)\rangle\vec{S} + \frac{1}{2}(\langle j_0(q)\rangle + \langle j_2(q)\rangle)\vec{L}\big],$$

where the $\langle j_n(q)\rangle$ denote the radial integrals of nth-order spherical Bessel functions, and $\vec{L}$ is the angular momentum operator. The values of these integral expressions can be found in tables for most atoms. In the usual case where the orbital angular momentum is fully quenched by the crystal field in the absence of spin-orbit coupling, the moment we observe will be determined by the spin moment with an additional small contribution due to spin-orbit coupling, i.e. we have [22]

$$M(\vec{q}) \cong -g\mu_B f(q)\vec{S} \quad \text{with} \quad f(q) = \langle j_0(q)\rangle + \frac{g-2}{g}\langle j_2(q)\rangle,$$

where $f(q)$ is the magnetic form factor that accounts for the shape of the magnetization cloud associated with the atomic spin and orbital variables.

If, on the other hand, the crystal field is very small and the spin-orbit coupling large, the total angular momentum $\vec{J} = \vec{L} + \vec{S}$ is well defined, which leads to the substitution $\vec{S} \to \vec{J}$ and slightly different expressions for g and $f(q)$ based on the Landé factor g_J [22]. Both situations nicely illustrate how the dipole approximation allows us to consider observables based on angular momentum algebra.

If there is only one type of magnetic ion in the sample, the magnetic response function simplifies to [22]

$$\mathcal{S}(\vec{q},\omega) = g^2\mu_B f^2(q)e^{-2W}\sum_{\alpha\beta}(\delta_{\alpha\beta} - \hat{q}_\alpha\hat{q}_\beta)S_{\alpha\beta}(\vec{q},\omega), \tag{16}$$

where $S_{\alpha\beta}(\vec{q},\omega)$ is now a reduced partial response function that excludes the g- and magnetic form factors, μ_B, and the Debye-Waller factor e^{-2W}.

Now we can use the dipole approximation to express the magnetic response function in terms of the spin operator S in the case of small spin-orbit coupling and an intermediate crystal field (or J for large spin-orbit coupling), i.e. [22]

$$S_{\alpha\beta}(\vec{q},\omega) = \sum_{jk} e^{\vec{q}(\vec{r}_k-\vec{r}_j)} \cdot \frac{1}{2\pi\hbar} \int_{-\infty}^{\infty} dt \langle S_\alpha^j S_\beta^k(t)\rangle e^{-i\omega t}. \tag{17}$$

If there is more than one magnetic atom in the sample, no reduced form is possible and one must consider a more involved expression, i.e. [22, 24, 25]

$$\mathcal{S}(\vec{q},\omega) = \sum_{\alpha\beta} (\delta_{\alpha\beta} - \hat{q}_\alpha \hat{q}_\beta) S_{\alpha\beta}(\vec{q},\omega) \tag{18}$$

with

$$\begin{aligned} S_{\alpha\beta}(\vec{q},\omega) = &\sum_{jk} g_j g_k f_j(q) f_k(q) e^{-W_j - W_k} e^{\vec{q}(\vec{r}_k-\vec{r}_j)} \\ &\cdot \frac{1}{2\pi\hbar} \int_{-\infty}^{\infty} dt \langle S_\alpha^j S_\beta^k(t)\rangle e^{-i\omega t}. \end{aligned} \tag{19}$$

In practice, the assumptions for the dipole approximation are often fulfilled and it is widely used, especially for materials where the magnetization density is carried by electrons localized in atomic-like orbitals. However, it is not always easy to determine whether its use is justified, and it can be difficult to find the magnetic form factors and g-factors that vary with q, and may need to be measured first in some additional experiments. We also note that the magnetic form factors written in the dipole approximation are not very accurate. Thus, it is sometimes necessary to work with the more general expression in terms of the Fourier transform of the magnetization vector.

2 Methods

The idea of this project is to consider entanglement detection and quantification in solids from both a theoretical and an experimental point of view.

In terms of theoretical efforts, it is very instructive and in many ways easier to study the entanglement structure present in solids when working with toy models and facilitating assumptions. This is why we begin by investigating entanglement witnesses based on collective angular momentum observables from a purely theoretical point of view. Starting with the general concept of witness construction from macroscopic observables, we look at existing criteria and strategies, and investigate generalizations for non-Hermitian collective operators.

However, working only with ideal or close-to-ideal systems is of limited interest in the study of real systems and phenomena, such as quantum criticality in complex many-body systems. Thus, the challenge is to see if and how we can utilize and customize existing entanglement witnesses, explore and accommodate for both theoretical and experimental limitations, and eventually combine our methods to better understand the physics of our system and improve our models. Now, the idea is to relate some theoretical entanglement witnesses to observables accessible to neutron scattering experiments, perform said experiments, and analyse the outcome. Here, we focus on neutron scattering experiments, and investigate the role of the quantum Fisher information as an entanglement witness. We must note that it is already rather difficult to perform any type of neutron scattering experiment, as this requires not only expertise with the experimental setup but also access to special facilities. Such access is quite limited. This is why the initial data of interest for this study was not taken specifically for the purpose of entanglement detection. Nevertheless, it has been very instructive to investigate the difficulties that arise in the process of obtaining observables relevant for entanglement studies, and to find strategies to overcome them in the prospect of facilitating future studies.

2.1 Thermodynamic observables as entanglement witnesses

In theory, constructing an entanglement witness is quite simple. All that is needed are criteria that are violated by at least one entangled state. The difficulty is then to optimize a given witness such that it detects as many entangled states as possible.

For the purpose of witnessing entanglement in solids, we will focus on thermodynamic observables and response functions such as energy, specific heat, or susceptibilities, or combinations thereof. Witnesses for these observables often depend on assumptions about the underlying spin system, and are defined at thermal equilibrium, or close to $T = 0$ K. Consequently, it is crucial to bear in mind the applicability and limitations of such assumptions. For models that are not well-known, the challenge is to work in the most general setting possible while still being able to make any meaningful statements.

To illustrate the process of constructing an entanglement witness, consider the energy E as an observable. We can find a witness based on the system's Hamiltonian,

$$W = E - \inf_{\Psi \in \mathfrak{S}} [\langle \Psi | H | \Psi \rangle], \tag{20}$$

where $\mathfrak{S}$ again denotes the set of separable states. For many spin models, this optimization is easy to perform. For systems in thermal equilibrium, the state can be written as $\tau = \frac{1}{Z} e^{\beta H}$ with $\beta = 1/k_B T$ and $Z = \mathrm{Tr}(e^{\beta H})$. Using this expression, it is possible to derive a temperature bound so that states with $T < T_E$ must be entangled [26].

To illustrate the process of constructing a witness from a Hamiltonian, consider the example given in [27] of the spin-$\frac{1}{2}$ Heisenberg Hamiltonian for a d-dimensional cubic lattice of N spins with an external magnetic field B

$$H^H = \sum_{\langle ij \rangle} s_x^i s_x^j + s_y^i s_y^j + s_z^i s_z^j + B s_x^i. \tag{21}$$

Minimizing the function $f^H(\vec{s}^A, \vec{s}^B) = \vec{s}^A\vec{s}^B + \frac{B}{2}(s_z^A + S_z^B)$ for the most general product state $|A\rangle|B\rangle$, i.e. minimizing

$$\begin{aligned}\langle A|\langle B|f^H(\vec{s}^A, \vec{s}^B)|A\rangle|B\rangle = \\ &\sin(2\theta_A)\cos(\phi_A)\sin(2\theta_B)\cos(\phi_B) \\ &+ \sin(2\theta_A)\sin(\phi_A)\sin(2\theta_B)\sin(\phi_B) \\ &+ \cos(2\theta_A)\cos(2\theta_B) \\ &+ \frac{B}{2}(\cos(2\theta_A) + \cos(2\theta_B))\end{aligned}$$

yields the energy bound

$$E_{\text{sep}}^{\min} = \begin{cases} -dN(1 + B^2/8) & \text{if } |B| \leq 4 \\ -dN(|B| - 1) & \text{else.} \end{cases}$$

Similar approaches can be used to find bounds for states of a particular entanglement depth based on linear witnesses [28, 29]. Without detailing the entire process, two useful observations from these approaches should be emphasized. One, it is generally possible to find a bound based on pure k-producible states by solving a k-body problem. Second, this bound can be extended to any mixed k-producible state because any linear function takes its maximum in a pure k-producible state which is an extremal point of the convex set formed by all mixed k-producible states [29].

In addition to the energy, there are many complementary macroscopic observables and response functions that can be investigated, such as the magnetic susceptibility considered in [30] and [31]. Here, we focus on observables that probe the spin and orbital angular momentum correlations, such as the magnetic response function that can be obtained from neutron scattering experiments because the neutron's magnetic moment is susceptible to both orbital and spin angular momentum. Consequently, we will focus on observables corresponding to Fourier-transformed spin-spin correlators of collective angular momentum operators

$$J_\alpha(q) = \sum_n e^{iqn} j_\alpha^{(n)}, \tag{22}$$

where q is a real phase.

For instance, if we can extract a quantity of the form

$$D(\vec{q}) = \sum_\alpha c_\alpha J_\alpha^\dagger(q_\alpha) J_\alpha(q_\alpha) \tag{23}$$

with the index $\alpha = x, y, z$, the wave-vector transfer $\vec{q}$, and the collective spin-spin correlators $J_\alpha^\dagger(q_\alpha)J_\alpha(q_\alpha) = \sum_{n<m} e^{iq_\alpha|n-m|}\langle j_\alpha^{(n)} j_\alpha^{(m)}\rangle$, we can essentially follow the approach described in [32] and consider the expectation value of

$$H(\vec{q}) = \frac{1}{2}(D(\vec{q}) + D(\vec{q})^\dagger) = \frac{1}{2}(D(\vec{q}) + D(-\vec{q})). \tag{24}$$

To find a bound for separable states, we can consider a pure product ansatz state

$$\rho_{\text{sep}} = |\Psi_1\rangle\langle\Psi_1| \otimes ... \otimes |\Psi_N\rangle\langle\Psi_N|. \tag{25}$$

Using the property that for such states

$$\langle j_\alpha^{(n)} j_\alpha^{(m)}\rangle = \langle j_\alpha^{(n)}\rangle\langle j_\alpha^{(m)}\rangle \tag{26}$$

we arrive at

$$\langle H(\vec{q})\rangle_{\rho_{\text{sep}}} = \sum_\alpha c_\alpha \sum_{n<m} \cos(q_\alpha|n-m|)\langle j_\alpha^{(n)}\rangle\langle j_\alpha^{(m)}\rangle. \tag{27}$$

Then we can use the fact that $|c_\alpha| \leq 1$ and that $|\cos(q_\alpha|n-m|)| \leq 1$ to find the bound

$$
\begin{aligned}
|\langle H(\vec{q})|\rangle_{\rho_{\text{sep}}} &\leq \sum_{\alpha} \sum_{n<m} \langle j_\alpha^{(n)}\rangle\langle j_\alpha^{(m)}\rangle \\
&= \sum_{\alpha} \frac{1}{2} \sum_{n} \Big[\Big(\sum_{n} \langle j_\alpha^{(m)}\rangle \Big)^2 - \sum_{n} \langle j_\alpha^{(m)}\rangle^2 \Big] \\
&\leq \frac{1}{2} \sum_{\alpha} (N-1) \sum_{n} \langle j_\alpha^{(m)}\rangle^2 \leq \frac{1}{2} N(N-1) j^2
\end{aligned}
$$

where we applied the Cauchy-Schwarz inequality

$$
\Big(\sum_{n} \langle j_\alpha^{(m)}\rangle \Big)^2 \leq N \sum_{n} \langle j_\alpha^{(m)}\rangle^2 \tag{28}
$$

and the property that

$$
\sum_{\alpha} \langle j_\alpha^{(m)}\rangle^2 \leq j^2. \tag{29}
$$

Thus we can create an entanglement witness that serves as both an upper and an lower bound, i.e.

$$
W(\vec{q}) = \frac{1}{2} N(N-1) j^2 \mathbb{1} \pm H(\vec{q}). \tag{30}
$$

Note that for different $\vec{q}$ witnesses of this type generally detect different states.

The above witness takes into account correlations between all particles in the system. However, it is also possible to derive a similar witness for particles with limited interaction distances. To illustrate, consider a ring of N particles situated at equal distances from one another. If we only consider interactions up to a distance w, we may write

$$
\langle H_w(\vec{q})\rangle_{\rho_{\text{sep}}} = \sum_{\alpha} c_\alpha \sum_{n} \sum_{1 \leq d \leq w} \cos(q_\alpha d) \langle j_\alpha^{(n)}\rangle\langle j_\alpha^{(n+d)}\rangle. \tag{31}
$$

Now we can divide our ring into $\left(\frac{N}{w}\right)$ groups with $d \in 1, ..., w$ and find a similar bound,

$$\begin{aligned}\langle H_w(\vec{q})\rangle &\leq \left(\frac{N}{w}\right)^2 \sum_\alpha \sum_d \langle j_\alpha^{(n)}\rangle\langle j_\alpha^{(n+d)}\rangle \\ &\leq \frac{1}{2}\left(\frac{N}{w}\right)^2 w(w-1)j^2 = \frac{1}{2}N^2\frac{w-1}{w}j^2,\end{aligned} \tag{32}$$

now solving an $\left(\frac{N}{w}\right)$-particle problem, for simplicity assuming that N is divisible by w.

2.2 Collective variances and the quantum Fisher information

In some cases, it is easier to work with nonlinear witnesses based on second or even higher-order moments. An additional advantage is that it is possible to obtain stronger entanglement criteria when working with nonlinear witnesses. In order to construct such witnesses for general collective observables of the form $O = O(\vec{q}) = \sum_n o^{(n)} e^{-i\vec{q}\vec{r}_n}$, we want to formally introduce collective variances and the quantum Fisher information, and point out their useful properties.

The *variance* of such a collective observable is defined as

$$(\Delta O)_\rho^2 \coloneqq \langle O^\dagger O\rangle_\rho - \langle O^\dagger\rangle_\rho\langle O\rangle_\rho = \mathrm{Tr}(O^\dagger O\rho) - \mathrm{Tr}(O^\dagger\rho)\mathrm{Tr}(O\rho), \tag{33}$$

where ρ is a density matrix. This variance has several useful properties, i.e. it is

1. positive for all quantum states and observables, $(\Delta O)_\rho^2 > 0$,
2. concave under mixing a quantum state, $(\Delta O)_\rho^2 \geq \sum_k p_k (\Delta O)_{\Psi_k}^2$ where $\rho = \sum_k p_k |\Psi_k\rangle\langle\Psi_k|$, as well as its own concave roof, $(\Delta O)_\rho^2 = \max_{p_k,|\Psi_k\rangle} \sum_k p_k (\Delta O)_{\Psi_k}^2$,
3. additive for quantum states composed of uncorrelated parties such as $\rho = \rho_1 \otimes \rho_2$ and single-body collective observables $O = o^{(1)} \otimes \mathbb{1} + \mathbb{1} \otimes o^{(2)}$, $(\Delta o)_\rho^2 = (\Delta o^{(1)})_{\rho_1}^2 + (\Delta o^{(2)})_{\rho_2}^2$.

Similar properties hold for covariances, i.e.

$$\mathrm{Cov}(\vec{O})_{jk} = \langle O_j^\dagger O_k\rangle_\rho - \langle O_j^\dagger\rangle_\rho \langle O_k\rangle_\rho.$$

The *quantum Fisher information* (QFI) can be viewed as a complementary quantity to this variance. In parameter estimation theory, the QFI can be used as a figure of merit to characterize the estimation of a parameter, and its inverse lower-bounds the variance of an estimator in what is known as the quantum Cramér-Rao bound. The formal definition of the QFI [33, 34] is

$$F_Q[\theta] := \mathrm{Tr}(\rho L_\theta^2) = \langle L_\theta^2\rangle \tag{34}$$

where L_θ is the self-adjoint symmetric logarithmic derivative operator (SLD) that fulfills

$$\partial_\theta \rho_\theta = \frac{1}{2}(\rho_\theta L_\theta + L_\theta \rho_\theta).$$

Tracing over this expression, $\mathrm{Tr}(\partial_\theta\rho_\theta) = 0 = \frac{1}{2}(\mathrm{Tr}(\rho_\theta L_\theta) + \mathrm{Tr}(L_\theta\rho_\theta)) = \mathrm{Tr}(\rho L_\theta) = \langle L_\theta\rangle$, it can be seen that the QFI must be the variance of L, i.e.

$$F_Q[\theta] = (\Delta L_\theta)^2. \tag{35}$$

For a density matrix written in its eigenbasis $\rho = \sum_k \lambda_k |k\rangle\langle k|$, the QFI can then be written as

$$F_Q[\theta] = 2\sum_{k,l} \frac{|\langle k|\partial_\theta\rho_\theta|l\rangle|^2}{(\lambda_k + \lambda_l)}$$

with $\lambda_k + \lambda_l > 0$ in the summation over k and l. Similar to the variance, the QFI is positive for all ρ and O, and additive for product states. Contrary to the variance, however, it is convex under mixing.

For states undergoing unitary perturbations, $\rho = U\rho_0 U^\dagger$, with $U = e^{-i\theta O}$ and $O = O^\dagger$, we have that $\partial_\theta\rho_\theta = iU[O,\rho_0]U^\dagger$, and the QFI can be written as [35]

$$F_Q[\rho, O] = 2 \sum_{k,l} \frac{(\lambda_k - \lambda_l)^2}{(\lambda_k + \lambda_l)} |\langle k| O |l\rangle|^2. \tag{36}$$

For pure states and Hermitian observables we have $\lambda_0 = 1$ and $\lambda_{i>0} = 0$. Hence,

$$\begin{aligned} F_Q[|\Psi\rangle\langle\Psi|, O] &= 2 \cdot 2 \sum_{k\neq 0} |\langle k| O |0\rangle|^2 \\ &= 4 \sum_{k\neq 0} \langle 0| O |k\rangle\langle k| O |0\rangle \\ &= 4 \langle 0| O \sum_{k\neq 0} |k\rangle\langle k| O |0\rangle \\ &= 4 \langle 0| O(\mathbb{1} - |0\rangle\langle 0|) O |0\rangle \\ &= 4(\langle 0| O^2 |0\rangle - \langle 0| O |0\rangle^2) \\ &= 4(\Delta O)^2 \end{aligned} \tag{37}$$

the QFI is equal to four times the variance. This important observation can be generalized to mixed states in terms of their pure-state decompositions

$$F_Q = 4 \min_{p_k, |\Psi_k\rangle} \sum_k (\Delta O)^2_\rho \tag{38}$$

with $\rho = \sum_k p_k |\Psi_k\rangle\langle\Psi_k|$. Thus, the QFI is actually the convex roof of the variance.

For non-Hermitian observables $O \neq O^\dagger$, similar results can be obtained, in particular

$$F_Q[|\Psi\rangle\langle\Psi|, O] = 4(\langle O^\dagger O\rangle_\theta - \langle O^\dagger\rangle_\theta \langle O\rangle_\theta),$$

which reduces to Eq. (37) if $O = O^\dagger$.

Now, both collective variances and the QFI can be used to construct entanglement witnesses.

Because the collective variance is additive on pure product states, we can find bounds for linear combinations of variances based on the sum of the local variances. Thus, it suffices to consider the problem restricted to a local subspace instead of heaving to deal with the global space.

There are two options to extend such variance bounds for pure states to all mixed states. One is to extend lower bounds by looking at the largest concave function of the variance, i.e. its concave roof; this is simply known as the variance itself. In fact, a whole set of linear inequalities based on such variances is known as generalized spin-squeezing inequalities. The other option is to extend upper bounds by looking at the convex roof, as is the idea of the QFI.

In general, we can note that inequalities based on the QFI are more likely to detect states close to pure states with a large values of some collective variance, whereas variance-based criteria are more likely to detect states close to pure states with small values of some collective variances, e.g. close to antiferromagnetic states. This is why these approaches should be viewed as complementary, and investigated separately.

In what follows, we will introduce both notions in some detail, and explore their connection to the neutron-scattering observable relevant to our experiment.

2.2.1 Generalized spin-squeezing inequalities

There exist well-known inequalities specifically designed for detecting entanglement based on the measurements of expectation values and variances of collective angular momentum operators Eq. (22). These are known as generalized spin-squeezing inequalities [36–38]. A complete set of such inequalities exists for spin-$\frac{1}{2}$ particles [39]. Further generalizations can be made for a system of N particles of arbitrary spin j, yielding a set of criteria

$$(N-1)\sum_{\alpha\in I}(\tilde{\Delta}J_\alpha(q_\alpha))^2-\sum_{\alpha\notin I}\langle\tilde{J}_\alpha^2(q_\alpha)\rangle+N(N-1)j^2\geq 0, \tag{39}$$

where I is a subset of indices of $\{x, y, z\}$ and $\langle \tilde{J}_\alpha^2(q_\alpha)\rangle$ is the modified second moment that is defined as

$$\langle \tilde{J}_\alpha^2(q_\alpha)\rangle \coloneqq \langle J_\alpha^2(q_\alpha)\rangle - \sum_n \langle (j_\alpha^{(n)})^2\rangle = \sum_{n\neq m} e^{iq_\alpha(m-n)}\langle j_\alpha^{(n)} j_\alpha^{(m)}\rangle \tag{40}$$

and where we used Eq. (29).

Every inequality in this set is fulfilled by all separable states.

Proof. To see that this holds, we can use a strategy very similar to our derivation of Eq. (32). Again, we begin by looking at the modified collective variance

$$(\tilde{\Delta} J_\alpha(q_\alpha))^2 = \sum_n \sum_{l=1}^{N} e^{-iq_\alpha l}\langle j_\alpha^{(n)} j_\alpha^{(n+l)}\rangle - \sum_n \sum_{l=0}^{N} e^{-iq_\alpha l}\langle j_\alpha^{(n)}\rangle\langle j_\alpha^{(n+l)}\rangle. \tag{41}$$

For product states Eq.(26) holds, and thus

$$(\tilde{\Delta} J_\alpha(q_\alpha))^2 = -\sum_n \langle j_\alpha^{(n)}\rangle^2. \tag{42}$$

Similarly, for product states we can write

$$\langle \tilde{J}_\alpha^2(q_\alpha)\rangle = \Big(\sum_n e^{-iq_\alpha n}\langle j_\alpha^{(n)}\rangle\Big)\Big(\sum_n e^{iq_\alpha n}\langle j_\alpha^{(n)}\rangle\Big) - \sum_n \langle j_\alpha^{(n)}\rangle^2, \tag{43}$$

and, using the Schwarz inequality in the form

$$\Big(\sum_n e^{-iq_\alpha n}\langle j_\alpha^{(n)}\rangle\Big)\Big(\sum_n e^{iq_\alpha n}\langle j_\alpha^{(n)}\rangle\Big) \leq \sum_n \left|e^{iq_\alpha n}\right|^2 \langle j_\alpha^{(n)}\rangle^2 = N\sum_n \langle j_\alpha^{(n)}\rangle^2, \tag{44}$$

the modified second moment is upper-bounded by

$$\langle \tilde{J}_\alpha^2(q_\alpha)\rangle \leq (N-1)\sum_n \langle j_\alpha^{(n)}\rangle^2. \tag{45}$$

From this, we can write that for product states, Eq. (39) becomes

$$-(N-1)\sum_{\alpha}\sum_{n}\langle j_{\alpha}^{(n)}\rangle^2 + N(N-1)j^2. \tag{46}$$

Because of Eq. (29), we see that Eq. (39) holds for product states. Since the left-hand side of this expression is concave, this proof can be extended to all separable states. ■

Note that this bound holds independently of q_α. Thus, we see that in this case it does not matter whether we consider collective operators with or without a local phase factor. Based on this observation, this notion may be extended to more general cases of $\vec{q}$-dependent collective operators.

2.2.2 The quantum Fisher information as an entanglement witness

The QFI is a popular witness for multipartite entanglement. To illustrate this point, consider that for any separable state and collective operator O, the following inequality holds [40]:

$$F_Q[\rho_{\text{sep}}, O] \leq 4(\Delta O)^2, \tag{47}$$

due to the convexity of the QFI and the concavity of the variance. For an ensemble of N spin-j particles, and a collective angular momentum operator $J_\alpha = \sum_k j_\alpha^k$ with $\alpha = x, y, z$, the maximum variance becomes $(\Delta J_\alpha)^2 = Nj^2$, and thus for pure states we have $F_Q[|\Psi\rangle\langle\Psi|, J_\alpha] \leq 4Nj^2$ [41]. Consequently, for separable states, $F_Q[\rho_{\text{sep}}, J_\alpha] \leq 4Nj^2$ holds as well. For general states, $F_Q \leq 4N^2j^2$ holds [42]. Importantly, the entanglement depth can be bounded by

$$F_Q \leq 4kNj^2, \tag{48}$$

such that if N is divisible by k a violation of this inequality indicates a depth of entanglement of at least $(k+1)$ [43].

Note that this bound may be trivially extended to collective spin operators Eq. (22). To see this, consider that for pure k-producible states of the form

$\bigotimes_n |\Psi_n\rangle$, where Ψ_n are states of k_n particles and $\sum_n k_n = N$, with N divisible by k, we have the following constraint for the maximum variance:

$$(\Delta J_\alpha(q))^2 = \sum_n (\Delta j_\alpha^{(n)}) \leq \sum_n k_n^2 j^2 \leq N k j^2. \tag{49}$$

Another aspect of experimental interest to our study is the fact that the QFI obeys universal scaling laws at very low temperatures that are linked to a diverging entanglement depth k, and a diverging universal entanglement length scale $l_{ent} \gtrapprox f_Q^{1/d}$ for $f_Q = F_Q/N \approx k$ [44].

2.2.3 Relation to the dynamic structure factor

Now that we know how (co-)variances and the QFI are generally useful in the construction of entanglement witnesses, let us explore how they are connected to neutron scattering observables in particular. From [44], it is known that under the assumption of thermal equilibrium

$$F_Q[\tau, O] = \frac{4}{\pi} \int_0^\infty d\omega \tanh\left(\frac{\beta\omega}{2}\right) \cdot \chi''_O(\vec{q}, \omega), \tag{50}$$

with

$$\chi''_O(\vec{q}, \omega) = \tanh \frac{\beta\omega}{2} \tilde{\mathcal{S}}(\vec{q}, \omega), \tag{51}$$

where $\tilde{\mathcal{S}}(\vec{q}, \omega)$ is the dynamical part of the structure factor given in Eq. (14).

Proof. For a thermal-state we have $\tau = \sum_n \lambda_n |n\rangle \langle n|$ with $\lambda_n = \exp(-\beta E_n)/Z$ and $Z = \sum_m \exp(-\beta E_m)$. Consequently, [44]

$$\frac{(\lambda_k - \lambda_l)}{(\lambda_k + \lambda_l)} = \tanh\left(\frac{\beta(E_l - E_k)}{2}\right) = 2 \int_0^\infty d\omega \tanh\left(\frac{\beta\omega}{2}\right) \delta(\omega + E_l - E_k). \tag{52}$$

Next, we consider the thermal-state expansion of the imaginary part of the dynamic susceptibility from linear response theory, $\chi''_{O_{kl}} = \sum_{nm} \pi\delta(E_m - E_n + \omega)(p_n - p_m) \langle n| O_k |m\rangle \langle m| O_l |n\rangle$.

Comparing the above expressions with the definition of the QFI in Eq. (36), one immediately obtains Eq. (50).

The imaginary part of the dynamic susceptibility is related to the dynamical structure factor as $\tilde{\mathcal{S}}(\vec{q},\omega) = \frac{\hbar}{\pi}\frac{1-e^{-\beta\omega}}{1+e^{-\beta\omega}} \cdot \sum_{k,l}(\chi''_{O_{kl}}(\vec{q},\omega) + \chi''_{O_{lk}}(\vec{q},\omega)) = \frac{1+e^{-\beta\omega}}{1-e^{-\beta\omega}}\chi''_O(\vec{q},\omega)$. Thus, $\chi''_O(\vec{q},\omega) = \frac{1-e^{-\beta\omega}}{1+e^{-\beta\omega}}\tilde{\mathcal{S}}(\vec{q},\omega) = \tanh\frac{\beta\omega}{2}\tilde{\mathcal{S}}(\vec{q},\omega)$. ■

Similar to the expression for the QFI in Eq. (50), it holds that, in thermal equilibrium,

$$\mathrm{Cov}(O)_\rho = \frac{1}{\pi}\int_0^\infty d\omega \coth\left(\frac{\beta\omega}{2}\right)\cdot\chi''_O(\vec{q},\omega). \tag{53}$$

Proof. First, we look at the expansion of the imaginary part of the dynamic susceptibility:

$$\begin{aligned}\chi''_{O_{k,l}}(\vec{q},\omega) &= \sum_{nm}\pi\delta(E_m - E_n + \omega)(e^{-\beta E_n} - e^{-\beta E_m})\langle n|O_k|m\rangle\langle m|O_l|n\rangle \\ &= \sum_{nm}\pi\delta(E_m - E_n + \omega)e^{-\beta E_n}(1 - e^{-\beta\omega})\langle n|O_k|m\rangle\langle m|O_l|n\rangle .\end{aligned}$$

Second, we can expand the covariance matrix of the operators $O(t) = e^{iHt}O(0)e^{-iHt}$ with $O(0) = O$ in terms of the energy eigenbasis,

$$
\begin{aligned}
\mathrm{Cov}(O_k(t), O_l(0))_\tau &= \frac{1}{2}\int_{-\infty}^{\infty} e^{i\omega t}\langle O_k(t)O_l(0) + O_l(0)O_k(t)\rangle \\
&= \frac{1}{2}\int_{-\infty}^{\infty} e^{i\omega t}\mathrm{Tr}(\tau e^{iHt}O_k(0)e^{-iHt}O_l(0) + \tau O_l(0)e^{iHt}O_k(0)e^{-iHt}) \\
&= \frac{1}{2}\int_{-\infty}^{\infty} e^{i\omega t}\sum_{n,m}(\langle n|\,\tau e^{iHt}O_k(0)e^{-iHt}\,|m\rangle\,\langle m|\,O_l(0)\,|n\rangle \\
&\quad + \langle n|\,\tau O_l(0)\,|m\rangle\,\langle m|\,e^{iHt}O_k(0)e^{-iHt})\,|n\rangle) \\
&= \frac{1}{2}\sum_{n,m} 2\pi(\delta(\omega + E_n - E_m)e^{-\beta E_n}e^{i(E_n-E_m)t}\,\langle n|\,O_k\,|m\rangle\,\langle m|\,O_l\,|n\rangle \\
&\quad + \delta(\omega + E_m - E_n)e^{-\beta E_n}e^{i(E_m-E_n)t}\,\langle n|\,O_l\,|m\rangle\,\langle m|\,O_k\,|n\rangle) \\
&= \sum_{n,m}\pi(\delta(\omega + E_n - E_m)e^{-\beta E_n}\,\langle n|\,O_k\,|m\rangle\,\langle m|\,O_l\,|n\rangle \\
&\quad + \delta(\omega + E_n - E_m)e^{-\beta(E_n+\omega)}\,\langle m|\,O_l\,|n\rangle\,\langle n|\,O_k\,|m\rangle) \\
&= (1 + e^{-\beta\omega})\sum_{n,m}\pi\delta(\omega + E_n - E_m)e^{-\beta E_n}\,\langle n|\,O_k\,|m\rangle\,\langle m|\,O_l\,|n\rangle \\
&= \frac{(1 + e^{-\beta\omega})}{(1 - e^{-\beta\omega})}\chi''_{O_{k,l}}(\vec{q},\omega) = \coth\left(\frac{\beta\omega}{2}\right)\chi''_{O_{k,l}}(\vec{q},\omega).
\end{aligned}
$$

■

2.3 A spin-squeezing inequality for non-Hermitian collective observables

In what follows, we want to focus on finding bounds for the range of entanglement. One approach to do so is based on the minimization of a two-particle variance for pure states and presented in [3]. This has motivated us to look for a similar bound on the range of entanglement as the solution of a two-body problem that can be related to neutron scattering observables. For this purpose, we take an approach based on the strategy of finding planar spin-squeezing criteria for the depth of entanglement presented in [45].

If the assumptions for the dipole approximation hold, we may consider the dynamic structure factor containing the correlators of collective spin operators as in Eq. (12) and (19). When working with the expression for the

magnetic neutron scattering cross section in the dipole approximation, one may consider the expression Eq. (18). From this, we consider the observable

$$\sum_{\vec{q}\in Q}\sum_{\alpha,\beta}(\delta_{\alpha\beta}-\hat{q}_\alpha\hat{q}_\beta)\Delta S_\alpha(q)\Delta S_\beta(q),$$

where the $S_\alpha(q)=\sum_{n=1}^{r}e^{iqn}j_\alpha^{(n)}$ for $\alpha=x,y$ are collective operators of r parties. Thus, we see only the squared expectation values of the collective operators perpendicular to $\vec{q}$. Without loss of generality we may then consider

$$(\Delta S_\perp(q))^2=(\Delta S_x(q))^2+(\Delta S_y(q))^2. \tag{54}$$

Consider now ansatz states of the form

$$\rho_P=\bigotimes_{(n,m)\in P}\rho_{nm} \tag{55}$$

where the ρ_{nm} are two-particle states and P is one pairing of particle indices. With this ansatz state, it holds that

$$(\Delta S_\alpha(q))^2=\sum_{(n,m)\in P}(\Delta j_\alpha^{nm}(q))^2_{\rho_{nm}} \tag{56}$$

with $j_\alpha^{nm}(q)=e^{iqn}j_\alpha^{(n)}\otimes\mathbb{1}+e^{iqm}\mathbb{1}\otimes j_\alpha^{(m)}$. Introducing $d=|m-n|$, we may write $j_\alpha^{n(n+d)}(q)=j_\alpha^{(n)}\otimes\mathbb{1}+e^{iqd}\mathbb{1}\otimes j_\alpha^{(n+d)}$ which leads to

$$\begin{aligned}(\Delta S_\perp(q))^2_N=\sum_{\alpha=x,y}\sum_{(n,n+d)\in P}\Big(&2(\Delta j_\alpha^{(n)})^2+2\cos(qd)(\langle j_\alpha^{(n)}\otimes j_\alpha^{(n+d)}\rangle\\&-\langle j_\alpha^{(n)}\rangle\langle j_\alpha^{(n+d)}\rangle)\Big)\end{aligned}$$

for pure k-producible states of N particles with a fixed depth of entanglement r at a given range of entanglement w. For simplicity, we also assume that the particles are arranged at equal spacing.

Following the idea of [46], generalized by [47], [48], and [45], we want to find bounds for such states of the form

$$(\Delta S_\perp(q))^2 \geq \frac{N}{2} G_w(\langle S_x(q)\rangle/N), \tag{57}$$

with

$$G_w(X) \coloneqq \min_{d\in\{1,\dots,w\}} \min_{\phi\in(\mathbb{C}^{(2j+1)})^{\otimes 2}} (\Delta S_\perp(q))^2_\phi, \tag{58}$$

such that $\langle S_x(q)\rangle_\phi = X$ for any given value of q. The function $G_w(\cdot)$ is convex and acts as a lower bound for the range of entanglement for a given combination of observables $(\Delta S_\perp(q))^2$ and $\langle S_x(q)\rangle$.

By definition of G_w, we have that for pure two-producible states of N particles and a range of entanglement w at fixed q, and for $0 < d < w$

$$\sum_{(n,n+d)\in P} (\Delta j_\perp^{n(n+d)}(q))^2 \geq \sum_{(n,n+d)\in P} G_d(\langle j_x^{n(n+d)}(q)\rangle). \tag{59}$$

The G_d are decreasing for increasing indices, i.e. $G_a < G_b$ for $a > b$ because in the latter case the minimization is performed on a larger space. Thus, we see that

$$\begin{aligned}\sum_{(n,n+d)\in P} G_d(\langle j_x^{n(n+d)}(q)\rangle) &\geq \sum_{(n,n+w)\in P} G_w(\langle j_x^{n(n+w)}(q)\rangle) \\ &\geq \frac{N}{2} G_w(S_x(q)/N),\end{aligned}$$

where for the last inequality we used that the G_d are convex functions and applied Jensen's inequality, i. e. that for any convex function g and probability distribution it holds that $g\big(\sum_i p_i x_i\big) \leq \sum_i p_i g(x_i)$.

To find $G_w(X)$, we minimize $(\Delta S_\perp(q))^2/N$ for every given value of $X = \langle S_x(q)\rangle_\rho/N$ and ansatz state ρ of a given depth and width. Following the ap-

proach detailed in [45], this directly translates into the optimization problem of finding the ground state $|\Psi_\lambda\rangle$ of the following Hamiltonian

$$H = S_x^\dagger(q)S_x(q) + S_y^\dagger(q)S_y(q) - \lambda \cdot \mathrm{Re}\{S_x(q)\}. \tag{60}$$

Once we have found this ground state, we can calculate the expectation values of the above observables. For a system of two spin-$\frac{1}{2}$-particles, this becomes

$$\begin{aligned} G_w &= (\Delta S_\perp(q))^2, \\ X &= \langle S_x(q)\rangle. \end{aligned} \tag{61}$$

Note that we can extend this method to general k-producible states and find bounds for the range of entanglement w and depth of entanglement r where it suffices to consider a subspace of r particles. We can repeat this procedure for any q and $\lambda \in \mathbb{N}$. Taking the convex hull of the set of points in the plane of $((\Delta S_\perp(q))^2/N, \langle S_x(q)\rangle/N)$ for every λ, we have found the boundary for all states.

To find the range of entanglement, we may consider ansatz states that are two-body entangled at an arbitrary range. For our purpose, this means that in order to compute the bound for a given bipartite state, all we need to do is to consider a specific q corresponding to the range that we are interested in, and plot the result for many values of λ. To illustrate, we consider the case where $q = \pi$ and $w = 2$ in Fig. 3, and note that this bound coincides with the bound for the case $q = 0$.

This indicates that in this case the bound of the depth coincides with the bound for the range. Here, we cannot find a separate bound for the range of entanglement based on the solution of a two-body problem. Instead, we will have to look at three-body or even r-body problems to find bounds for the range of entanglement.

We further note that to verify the depth of entanglement r, it is generally necessary to look at all $\frac{N!}{r!(N-r)!}$ combinations of r particles along our string

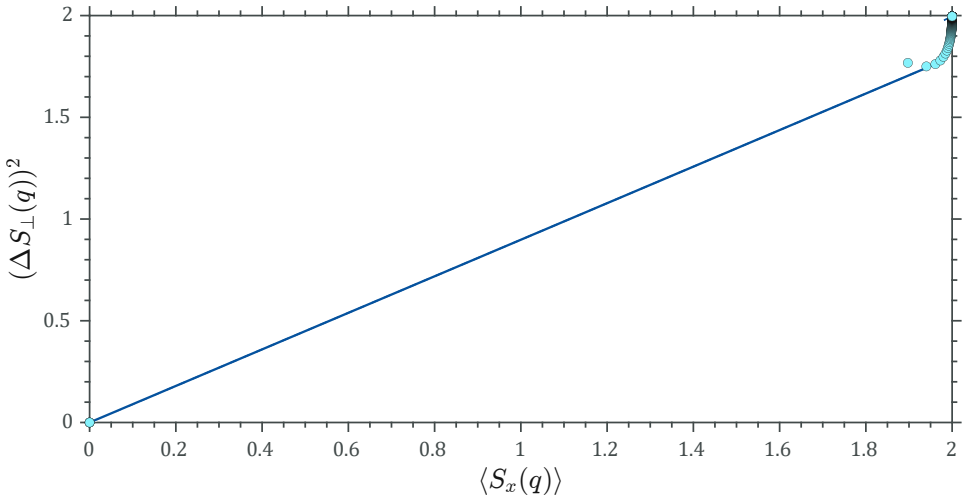

Figure 3: $G_2(X)$ for $q = \pi$. The figure shows the convex roof (dark blue line) of the set of points in the plane given by $((\Delta_\perp S(q))^2, \langle S_x(q)\rangle)$ calculated for $\lambda \in [0, 500]$.

with N being the total number of particles. In the case of a bipartite system, this corresponds to optimizing over all possible values of dq. For $r > 2$, this would generalize to probing all possible combinations of r-body entangled states for all $q \in 2\pi\frac{n}{N}, n \leq r$.

2.4 Experimental neutron scattering

In order to obtain the dynamic structure factor from the magnetic scattering cross section, we perform our measurements at the ThALES experiment at the ILL. The setup in Fig. 4 consists of a triple axis spectrometer setup, magnets, and cooling. First, the incoming cold neutrons traverse the velocity selector and monochromator that allow only neutrons with an energy of $E_i \pm \Delta E$ to proceed to the first collimator and diaphragm that focus the beam onto the sample. The sample itself is placed on a sample holder inside a magnetic field, and may be rotated by any angle. Both sample and sample holder are cooled using liquid helium. The neutrons that traverse the sample proceed to the analyzer, a rotating monochromator, that allows only neutrons

with a specific energy to hit the detector. That way, energy-resolved count rates can be obtained.

ThALES operates at high neutron-flux rates and very low background. Thus, it is ideal for the study of magnetic materials, as it can resolve even weak signals in low-temperature environments. ThALES also allows the users to perform experiments with polarized neutrons.

Throughout our experiments, the initial energy and orientation of the incoming neutrons are fixed, and the outgoing neutrons' energy and position are measured with a time-of-flight detector. The neutrons traverse bulk samples of strange metal compounds.

2.4.1 Practical considerations

First, the sample needs to be prepared. Since it is often quite difficult to produce the compounds of interest in good quality, samples are often small and uneven. Once prepared, the sample is mounted onto a sample holder with a goniometer, and placed on a rotating axis inside a cooling cell and a magnetic field.

Prior to the actual measurements, the sample needs to be aligned. If the crystal structure is known, this means finding a Bragg peak along which to orient the crystal and define the orientation and origin of the (h, k, l)-plane. If the sample consists of multiple samples glued together, the internal alignment is also important to consider. For instance, multiple Bragg peaks may appear in misaligned samples. Once the alignment has been completed and the scattering plane is defined, we can proceed with our measurements.

Regarding these measurements, another important consideration is that we do not directly measure Eq. (6) but rather the scattering intensity that can in practice be approximated as [49]

$$I(\vec{q}, E) = \frac{d^2\sigma}{d\Omega dE} R_0(\vec{q}, E), \tag{62}$$

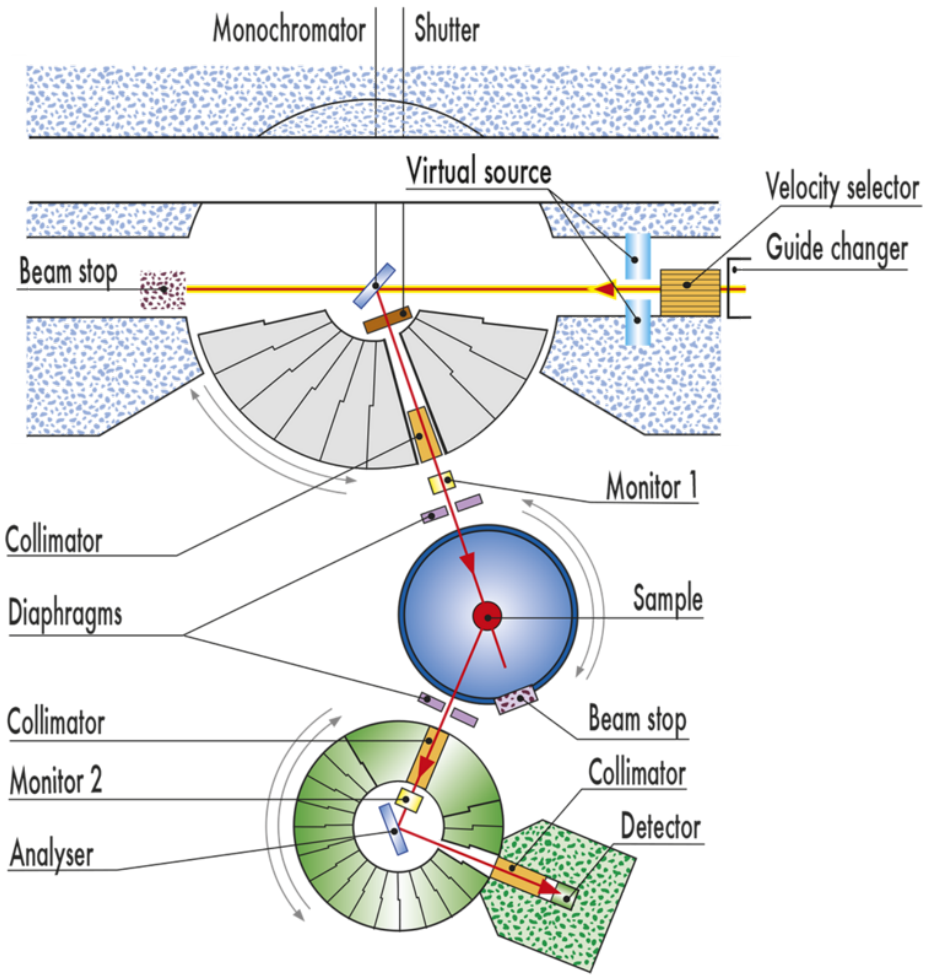

Figure 4: The Three Axis Low Energy Spectrometer (ThALES). The image was taken with permission from the ThALES instrument's website, last accessed on October 20 at https://www.ill.eu/users/instruments/instruments-list/thales/description/instrument-layout.

where $R_0(\vec{q}, E)$ is the resolution volume which only depends on the instrument. The limited instrumental resolution results mainly from the finite beam divergence and mosaicity of the monochromator crystals. In practice, this is written as the resolution ellipsoid and needs to be known in order to perform measurements in the focusing direction, i.e. the direction where the energy dispersion relation is in alignment with the tilt of the ellipsoid. This resolution volume can be calculated theoretically (for instance using the takin package), or simulated numerically with the help of Monte-Carlo methods. In general, the resolution volume is described as a tilted cigar-shape in phase space. At the instrument, it is then measured using a vanadium standard that scatters isotropically.

Regarding the resolution, one must also compare the resolution of the instrument to the energy scale of interest, i.e. is the experimental resolution good enough for the energies that we are interested in? In our case, we are interested in the quasi-elastic features close to zero meV. With ThALES, it is possible to obtain good resolution in the sub-meV regime.

Lastly, concerning the resolution and instrumental effects, we must consider that the experimental Gaussian is not a perfect Gaussian but has "feet" resulting from the monochromator that generally overlap with the quasi-elastic part of the cross-section. In our case, these feet are assumed to be much smaller than the quasi-elastic contribution.

Normalization

For quantitative analysis, the data obtained needs to be normalized. Normalization methods generally require extra measurement time and good knowledge of the sample and reference properties. Consequently, normalization procedures can be quite involved and are not usually carried out in practice unless absolutely necessary. Unfortunately, such infrequent usage also means that there are no systematic studies of the accuracy and robustness of these protocols. This is important information that must be individually evaluated for every method and every experiment. Standard procedures are described in [49] and include normalization based on sample

incoherent scattering, phonon coherent scattering, and vanadium incoherent scattering.

The first of these methods is quite simple, as all that is needed is the measurement of the sample incoherent elastic scattering, i.e. an energy scan far away from any Bragg peaks, and the values for the incoherent elastic scattering cross section of the sample atoms that can be obtained from the literature. Note that the normalization is performed per unit cell; it may need to be rescaled to the number of magnetic atoms in the unit cell. This method is not advisable in case the incoherent elastic scattering contribution from the sample is small compared to the contributions from the sample holders and environments, which can lead to a significant over-estimation of the normalization factor [49]. This is why we favour the use of the following more robust protocols.

While we cannot normalize the data from the $Ce_3Pd_{20}Si_6$ measurements without performing the experiment again, this has been of special relevance for the $CeRu_4Sn_6$ measurements where we could select a protocol. We had decided to measure both a phonon and the vanadium standard as both methods are known to be robust, and it would have been interesting to compare the result. Unfortunately, there were some complications during the experiment and we ended up not having enough time to find a phonon, leaving only the vanadium reference.

Because the incoherent cross-section of vanadium is much larger than its coherent counterpart, it is often used as a normalization standard. Following [49], we scanned the elastic line of vanadium, see Fig. 5, and divided the energy-integrated intensity I_{vanadium} by the theoretically calculated incoherent scattering cross-section for all the atoms in the unit cell, i.e. $\sigma^{\text{inc}} = \sum_j \sigma_j^{\text{inc}} e^{-2W_j}$, where e^{-2W_j} is the Debye-Waller factor that is assumed to be ≈ 1. This way, we obtain the normalization factor for vanadium,

$$N_{\text{vanadium}} k_f R_0 = 4\pi I_{\text{vanadium}} / \sigma^{\text{inc}}, \tag{63}$$

where N_{vanadium} is the number of unit cells in the vanadium sample, and k_f is the outgoing neutron wave-vector.

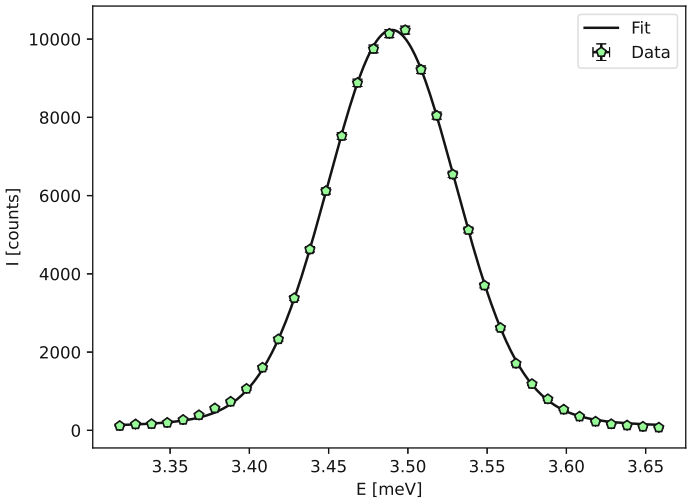

Figure 5: Scattering from the vanadium standard sample.

Because the resolution volume R_0 depends only on the instrument and not on any sample specifics, we can rescale the normalization to our sample based on the mass of the vanadium m_{vanadium} and the mass of our sample m_{sample}, i.e.

$$N_{\text{sample}} k_f R_0 = N_{\text{vanadium}} k_f R_0 \cdot \frac{m_{\text{sample}}}{m_{\text{vanadium}}}. \tag{64}$$

Note that we also need to convert the measured intensity to meV^{-1}, i.e. the intensity needs to be multiplied by $13.77(\text{b}^{-1})$. To obtain the dynamic structure factor, the intensity needs to be further deconvoluted, resulting in dividing the intensity by $g^2 e^{-2W} |f(Q)|^2$, where g is the g-factor, e^{-2W} is the Debye-Waller factor, and $f(Q)$ is the magnetic form factor.

Note that due to delays and complications during the experiment, normalizing the data is still a work in progress, the results of which will be shown in future works.

2.5 $Ce_3Pd_{20}Si_6$

In this thesis, we look at the data obtained from the $Ce_3Pd_{20}Si_6$ scattering experiment. To motivate our analysis and further our understanding of the underlying physics, we would like to introduce this compound.

2.5.1 Previous studies

$Ce_3Pd_{20}Si_6$ is an inter-metallic compound and an example of a strongly correlated electron system. The Ce^{3+}-ion has a single localized $4f$ electron with total angular momentum $J = \frac{5}{2}$. The crystal structure, shown in Fig. 6 (a), has two Ce sites formed by Ce1 at the $4a$ Wyckoff position arranged in a simple cubic (sc) lattice inside a face-centered cubic (fcc) lattice formed by Ce2 at the $8c$ Wyckoff position. In the appendix of [50], it is explained how the crystallographic ordering is determined by the atoms at the $8c$ site, whereas the 4a site is magnetically silent. Consequently, only the sc sublattice is of interest to us. For this sublattice, the grounds state is given by a Γ_8 quartet that includes three dipoles, five quadrupoles, and seven octupoles that give rise to dipolar and quadrupolar ordering via the RKKY interaction. Its spin and orbital states may be described in terms of two pseudospin operators, σ and τ, acting on the Kramers and non-Kramers doublet states. The interaction of the local moments with the conduction electrons through Kondo coupling and with each other through RKKY exchange may then be understood in terms of the multipolar Kondo model.

The multipolar Kondo model

The multipolar Kondo lattice model [50] is characterized by the Hamiltonian

$$H_{KL} = H_f + H_K + H_c. \tag{65}$$

The first term describes the RKKY-interaction among the local moments of the Γ_8 quartet characterized by I_{ij}^{κ} for $\kappa = \sigma, \tau, \sigma \otimes \tau$. The second term corresponds to the Kondo coupling between these local moments and the

conduction electrons characterized by J_K^κ. The last term represents the kinetic energy of the conduction electrons.

In extended dynamical mean-field theory, we look at the multipolar Bose-Fermi Kondo (BFK) model as an effective model for the Kondo lattice with the corresponding Hamiltonian [50]

$$H_{BFK} = H_K + H_{BK} + H_{B0}(\Phi_\sigma, \Phi_\tau, \Phi_{(\sigma\otimes\tau)}). \tag{66}$$

As in the Kondo lattice Hamiltonian, H_K describes the Kondo coupling between the local moments and the conduction electrons. The second term describes Bose-Kondo coupling between the local moments and the bosonic baths whose dynamics are specified in the last term.

The ground state of this model is described by a fully Kondo-screened many-body singlet, and has SU(4) symmetry [50], as can be seen in Fig. 6 (b). Its time evolution can be studied with the help of the hybridization-expansion continuous-time quantum Monte-Carlo method, in which the localization-delocalization transitions of the spin and orbital degrees of freedom are determined from calculations of their respective Binder cumulants. From these studies, the zero-temperature phase diagram can be obtained. Kondo destruction can be understood as a two-stage process in which the fully Kondo entangled phase breaks up into a fully spin-screened phase at the second QC point, and into a Kondo destroyed phase at the first QC point. In the destroyed phase, the material is antiferromagnetic, while it is antiferroquadrupolarly ordered in the screened phases.

2.5.2 Quantum criticality

$Ce_3Pd_{20}Si_6$ exhibits two QC points. The QC point emerging at 1.73 T separates two distinct antiferroquadrupolar (AFQ) phases. It is of particular interest to us because this is where our data were taken. However, it is also known that there is another QC point at a lower field value that marks the transition from an antiferromagnetic (AFM) phase at lower fields to an AFQ phase at higher fields than the critical field value. The QC points

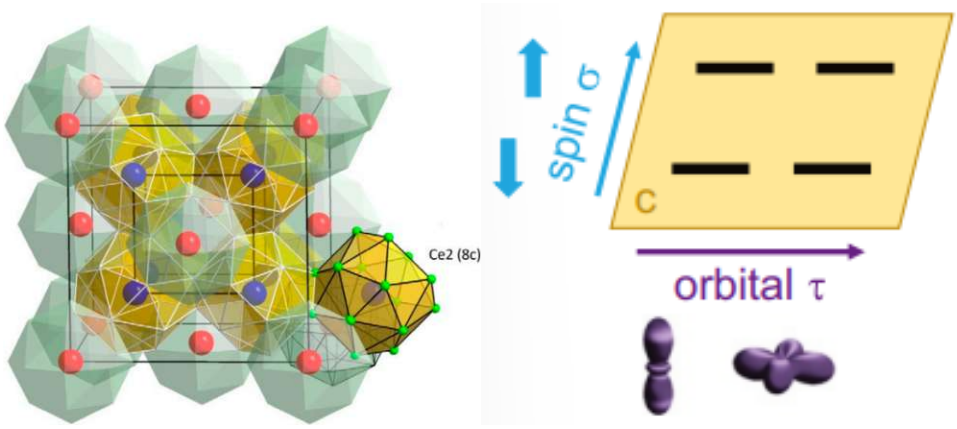

(a) Crystal structure (b) Ground state

Figure 6: (a) Cubic crystal structure of $Ce_3Pd_{20}Si_6$ taken from [50]. The lattice parameter is $a = 12.275$ Å. The Ce1 site at $4a$ is shown in red, the Ce2 site at $8c$ in blue. The polyhedra around Ce1 are formed by both Si and Pd, those around Ce2 by Pd. (b) Schematic ground state of the Γ_8 quartet as described in [50].

may be understood as marking the transition from fully Kondo entangled states to Kondo destroyed states where orbital and spin entanglement vanish consecutively [50]. In a heavy-fermion compound, Kondo entanglement describes a state where the localized 4f-electron degrees of freedom couple to the conduction electron's orbital and spin degrees of freedom. The QC phase can be characterized by a universal critical resistivity exponent, as is illustrated in Fig. 7.

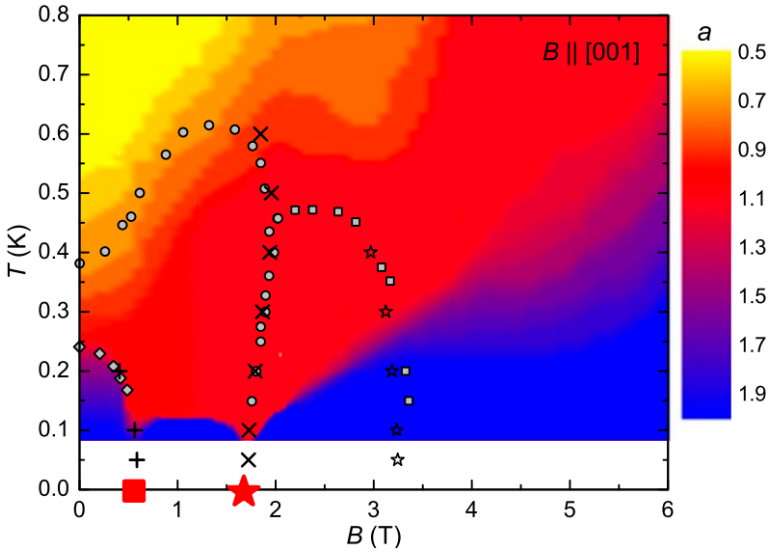

Figure 7: Temperature-magnetic field phase diagram taken from [50] of $Ce_3Pd_{20}Si_6$ for B = $\mu_0 H$k[0 0 1] . The colour corresponds to the resistivity exponent of ρ^{el} = $\rho_0^{el} + A_0 \cdot T^a$.

2.6 Data analysis

The scattering data of the $Ce_3Pd_{20}Si_6$ consist of several measurements taken at different temperatures ranging from 0.06 K to 10 K, at a fixed orientation $(h, k, l) = (0, -1, 0)$, i.e. away from any Bragg peaks, and at magnetic field values from 1.5 to 1.8 T, i.e. those close to the second QC point emerging at 1.73 T for $T = 0$ K.

Each measurement file contains the number of neutron counts at different energies. For each temperature, there exist three files containing two measurements to be averaged and an elastic line scan. The empty cryostat background was also measured and needs to be subtracted from all other measurements. Error bars are calculated based on Poisson statistics, i.e. the error scales as $\sqrt{N}$ where N is the number of counts for single measurements, and a weighted average for multiple measurements.

Next, the data is fitted using a sum of a Gaussian that accounts for the instrumental resolution around the elastic peak, and a Lorentzian that models the broadening due to diffusion. In practice, it is not easy to correctly separate the two contributions, as the exact resolution function is unknown. For our purposes, it is important not to over-estimate the Lorentzian contribution. Thus, we find the maximum Gaussian that can be fitted to all temperatures, and apply this to all other measurements. An example of such a fit is shown in Fig. 8.

We can then use these fits to divide the elastic and quasi-elastic contributions of the neutron-scattering profile. In particular, the fits allow us to look at the dynamics, i.e. the dynamic structure factor which can be extracted from the data minus the Gaussian (Fig. 9). From this dynamic structure factor, one can further calculate the magnetic dynamic susceptibilities (Fig. 10) and the QFI (Fig. 12).

Note that it would generally be useful and interesting to compare the data measured in the QC regime with data measured away from it, in different (separable) phases, especially if the data cannot be normalized. For this purpose, we looked at old measurements taken at different $\vec{q}$ in the material.

Unfortunately, the data was too sparse in the energy range that we were interested in, and it was not possible to perform the same kind of analysis due to the significant statistical error.

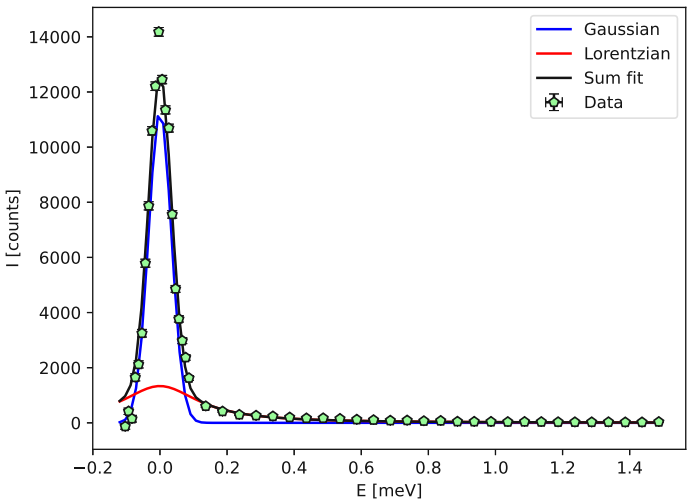

Figure 8: Fitting of Gaussian and Lorentzian of the lowest temperature sample.

3 Experimental results

In this analysis, we extracted the quasi-elastic part of the scattering cross section and see how this dynamic structure factor, in arbitrary units, illustrated in Fig. 9, and its derived quantities scale with different temperatures, i.e. the imaginary part of the susceptibility in Fig. 10 and the QFI integrands in Fig. 11. The structure factor and imaginary susceptibility are largest at low temperatures, while getting suppressed as T increases, which generally leads to the QFI being maximum at low temperatures, and decaying towards higher temperatures, as can be seen in Fig. 12. This behaviour appears to be consistent with the expectations from scaling theory.

Note that the QFI has been calculated from the data points minus their Gaussian fit values, the lines are based on the Lorentzian fit and shown for illustration purposes.

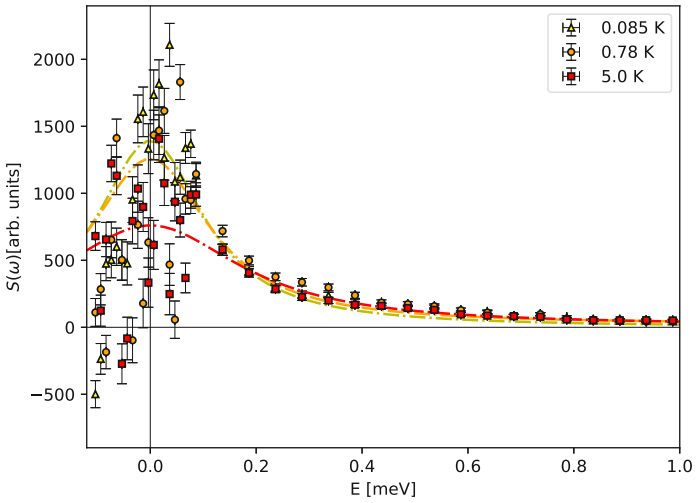

Figure 9: Scaling of the dynamic structure factor at different temperatures. The lines represent the Lorentzian fits, whereas the data points correspond to the respective data points minus their Gaussian fit value.

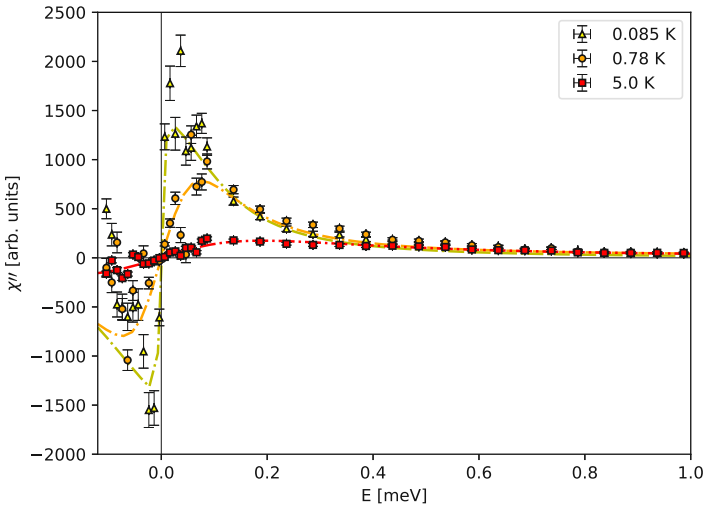

Figure 10: Imaginary parts of the dynamic susceptibility at different temperatures. The lines illustrate the imaginary part of the dynamic susceptibility again calculated based on the Lorentzian fits, whereas the data points correspond to the calculation based on the data points minus their Gaussian fit value.

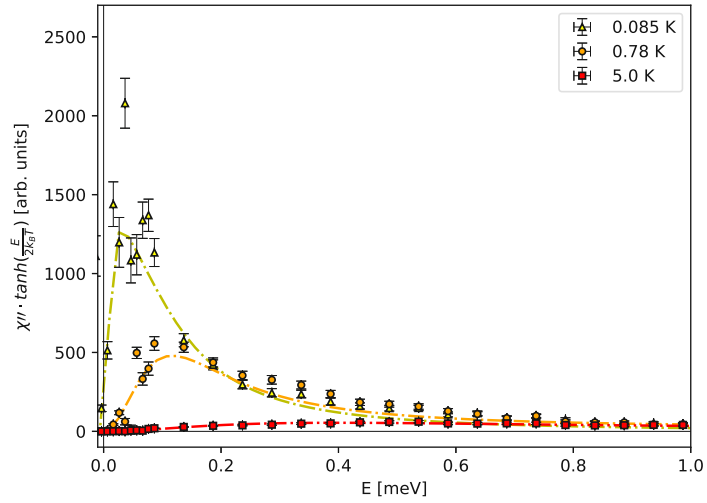

Figure 11: Integrand of the QFI at different temperatures. The lines show the integrand of the QFI based the Lorentzian fits, while the data points correspond to the calculation based on the data points minus their Gaussian fit value.

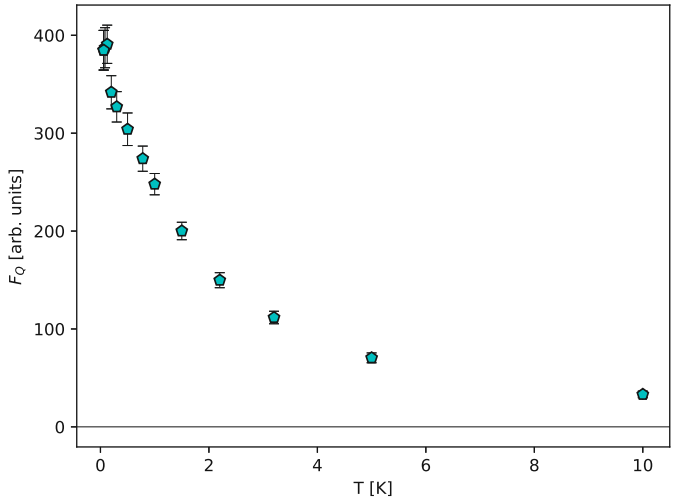

Figure 12: F_Q at different temperatures in arbitrary units.

4 Discussion

The presence and temperature scaling of quasi-elastic scattering in $Ce_3Pd_{20}Si_6$ indicates that this and related strange-metal compounds featuring KD QC points are good candidates for exploring entanglement structures close to quantum criticality.

For this purpose, we investigated how to probe entanglement in general solid state systems based on thermodynamic quantities. The applicability of any type of witnesses depends very much on the complexity of the system. If the compound is more complex, it is necessary to work with more general assumptions and observables. In particular when working with neutron scattering observables, we note that in systems where the dipole approximation is a good assumption, it is possible to decouple the spin-spin correlators from the cross section and use angular momentum algebra and spin squeezing inequalities to construct witnesses. Regarding witnesses based on collective operators, we observe that strategies used in the derivation of bounds for Hermitian collective observables can be extended to the non-Hermitian case. This allows for the generalization of existing inequalities to these more general observables, such as the bound on the QFI or spin-squeezing inequalities. While these inequalities hold for general collective observables of the form Eq. (22), different phase factors q enable the detection of different states. This may be useful in experimental setups that can probe different q, such as neutron scattering.

Building on these theoretical insights, we focused on experimentally obtaining the QFI from neutron scattering observables. In theory, the QFI allows one to witness the entanglement depth of some entangled states, which is directly related to the minimum range of entanglement. Hence, higher values for the depth of entanglement also indicate longer ranges of entanglement. Experimentally, we must note that the data obtained for $Ce_3Pd_{20}Si_6$ is not suitable for quantitative analysis due to it not being in absolute units. Thus, we cannot actually determine whether the material is entangled or not. However, considering the QFI in arbitrary units, we observe interesting scaling behaviour with temperature. We note that this behaviour is similar

to what has been obtained following a similar protocol in [8, 10] in the case of compounds modelling Heisenberg spin chains.

To improve upon these results, we planned and conducted a follow-up experiment investigating a similar compound, $CeRu_4Sn_6$, where we focused on probing the predicted zero-field quantum criticality, and on measuring the dynamic structure factor and its derived quantities in absolute units. However, due to unfortunate complications and a delay in the experiment, the analysis is more involved than in the case of $Ce_3Pd_{20}Si_6$ and will be the subject of futures studies.

5 Conclusion

This thesis investigated the possibilities and problems that arise in detecting and quantifying entanglement in a solid, attempting to better understand the limitations of both theory and experiment, as well as the role of assumptions and models in deriving entanglement witnesses.

In the theoretical part of this thesis, we explored how to derive entanglement witnesses based on collective angular momentum observables. Building on existing witnesses and protocols, we explored their connection to neutron scattering observables and argued that we can extend witnesses based on generalized spin-squeezing inequalities and the QFI to the case of non-Hermitian collective observables.

The experimental focus of this thesis is to look for entanglement in the neutron scattering data of $Ce_3Pd_{20}Si_6$. While this study was not able to verify and quantify entanglement in this compound, it may serve as a starting point for further investigations and more conclusive experiments. In particular, we highlight the importance of obtaining observables, such as the dynamic magnetic structure factor, in absolute units to allow for quantitative analysis, and we have explained how this can be done. Analysing our scattering data, we could extract the dynamic structure factor in arbitrary units and observe how this factors and its derived quantities scale with different temperatures at the critical magnetic field value.

6 Outlook

Because entanglement detection and quantification in solid state physics is a relatively novel field, this thesis concludes with an overview of some interesting ideas, related concepts, and experimental opportunities.

6.1 Experimental methods

Aside from (polarized) inelastic neutron scattering, there exist several other techniques useful for the extraction of observables based on spin-spin correlators and collective angular momentum observables. Back-scattering spectroscopy and neutron spin echo such as MIEZE [51] may be of particular interest due to the high energy resolution that can be achieved. In addition, it may be worthwhile to additionally measure the transverse magnetization using polarized neutrons. However, these methods also have drawbacks that one must consider, most importantly a significant loss of intensity when working with polarized neutrons or spin echo, and the loss of $\vec{q}$-dependence in a back-scattering setup. The intensity loss may be countered, to some extent, by longer measurement times to obtain reasonable statistics.

Another interesting approach would be to use entangled neutron beams to probe entanglement. In fact, an entire framework describing this method is presented in [52] and related works.

Naturally, other experimental approaches that are not based on neutrons are also being investigated. Of special interest would be methods based on local probes, as we will discuss in Section 6.3, or methods that allow us to directly probe second or higher-order spin-spin correlators such as spin-noise spectroscopy (SNS) [53].

6.2 Models and simulations

From a simulations point of view, it is interesting to study experimental testbeds such as frustrated Hamiltonians and topological systems due to their use in describing many physical phenomena of interest that are of experimental

relevance and go beyond the typically considered simplifications of the spin-spin Heisenberg models.

Note that it is generally possible to find a Hamiltonian that simulates the physics of a given strongly correlated system in a toy-model setup and numerically study it, for instance with RG analysis and QMC methods, as is done in [54] for a spin-$\frac{1}{2}$-Heisenberg chain coupled via a Kondo interaction to two-dimensional Dirac fermions. Their model Hamiltonian is written in second quantization as [54]

$$H = -t \sum_{\langle i,j\rangle,\sigma} (e^{\frac{2\pi i}{\phi_0}\int_i^j \mathbf{A}\mathbf{dl}} \mathbf{c_i}^\dagger \mathbf{c_j} + h.c.) + \frac{J_k}{2} \sum_{l=1}^{L} \mathbf{c_l}^\dagger \sigma \mathbf{c_l} \cdot \mathbf{S_l} + J_h \sum_{l=1}^{L} \mathbf{S_l} \cdot \mathbf{S_{l+\Delta l}},$$

where the first term describes the electron hopping with a tunable gauge factor, the second term describes the AFM Kondo coupling between the conduction electrons and the adatoms, and the third term describes the Heisenberg coupling between the adatoms.

It is indeed more challenging to find bounds similar to Eq. (2.1) for this Hamiltonian.

An obvious drawback in deriving witnesses based on Hamiltonians, however, is that such an approach requires knowledge of the Hamiltonian. Indeed, any such method can only be as good as the model describing the physics of the system. Thus, while entanglement witnesses based on this measure could lead to a better understanding of our numerical model and its limitations, they will not teach us any new physics outside of the model under consideration.

6.3 Local probes of entanglement

Instead of using global macroscopic observables, it may also be possible to measure local observables and construct witnesses based on those. For instance, using the additivity of the QFI, we have that for a bipartite state $\rho_{12} = \rho_1 \otimes \rho_2$ where $O_{12} = O_1 \otimes \mathbb{1} + \mathbb{1} \otimes O_2$ to be separable the following inequality must hold

$$F_Q[\rho_{12}, O_{12}] \leq 4[(\Delta O_1)^2_{\rho_1} + (\Delta O_2)^2_{\rho_1}].$$

This concept can be expanded to general partitions and the sum of the variances of the corresponding local operators. If the bound is violated, there exists entanglement between different partitions of the system. Thus, this inequality can in theory be used to verify the range of entanglement between distant partitions of a system.

When working in a continuous setting, we can define O as the Fourier transform of a generally non-Hermitian collective observable, i.e. $O = O(q) = \int dx e^{-iqx} O(x)$. We can further discretize the continuous space into small regions $1, 2, ..., n$ where we have $\rho = \sum_i p_i (\bigotimes_{n=1}^{N} \rho_n)_i$. By checking the entanglement bounds across all possible partitions of this quasi-discrete space, we can determine whether the regions feature entanglement beyond classical correlations. This way, we can probe how homogeneous the entanglement structure of a larger system is.

Is it experimentally possible to access subregions of a sample instead of the entire sample in order to probe the spatial distribution of entanglement? Considering a lattice of N sites, one may coarse-grain it by considering clusters of M sites grouped together in this lattice. Long-range entanglement would remain unperturbed by the clustering process. In neutron scattering experiments, the propagation of the neutron beam is described using the laws of geometrical optics. Similar to lasers or beams of charged particles, it is possible to narrow the incoming neutron beams using an aperture. This way, one may produce a neutron beam with a diameter of a few millimeters. In combination with a thin homogeneous sample of a few centimeters in diameter and collimation of the outgoing beam, this could be a viable starting point. However, several difficulties remain. One, defining an interaction volume remains difficult because the neutrons do not generally interact with all the atoms in the sample, and one must consider the effects of absorption and interaction with the environment and sample holder. Second, an important experimental consideration is the loss of intensity due to fewer neutrons reaching the sample. Bearing in mind that the error in measuring

the scattering intensity scales as $\sqrt{N}$, with N being the number of detector counts, it becomes more difficult to obtain good statistics at lower count rates. Third, it may be very difficult or even impossible to synthesise appropriate samples of the compounds we want to investigate for this type of experiment.

At present, we are limited to global measurements as we are dealing with small bulk samples that are assumed to be completely penetrated by the neutron beam. It would not be reasonable to steer the beam in such a way that the neutron-sample interaction would be limited to a specific volume within the sample.

An alternative approach worth mentioning, however, is to probe such samples with photons or electrons instead of neutrons. Unlike neutron beams, photon beams are often easier to control and focus. There exist several techniques to probe only specific regions of a sample, such as M-EELS [55], which achieves meV-resolution. The imaginary part of linear response functions

$$\chi_{OO}(x, x', t, t') = -i\langle[O(x, t)O(x', t')]\rangle\theta(t - t')$$

can be probed with scattering experiments. Whereas in neutron scattering we consider the spin response with $O = S$, in M-EELS one may look at the charge-density response with $O = \rho$. Note that the charge density response is not the same as the electron-density response, and that the former is directly related to the density-density correlation function, i.e. the charge structure factor. Thus, electrons may be used to probe charge entanglement.

References

[1] Bei Zeng, Xie Chen, Duan-Lu Zhou, and Xiao-Gang Wen, *Quantum Information Meets Quantum Matter – From Quantum Entanglement to Topological Phase in Many-Body Systems,* arXiv:1508.02595 [cond-mat.str-el] (2018).

[2] Andreas Osterloh, Luigi Amico, Giuseppe Falci, and Rosario Fazio, *Scaling of entanglement close to a quantum phase transition,* Nature **416**, 608 (2002), arXiv:quant-ph/0202029.

[3] Sabine Wölk and Otfried Gühne, *Characterizing the width of entanglement,* New J. Phys. **18**, 123024 (2016), arXiv:1507.07226.

[4] Zhihong Ren, Weidong Li, Augusto Smerzi, and Manuel Gessner, *Metrological Detection of Multipartite Entanglement from Young Diagrams,* Phys. Rev. Lett. **126**, 080502 (2021), arXiv:2012.03862.

[5] Barbara M. Terhal and Paweł Horodecki, *Schmidt number for density matrices,* Phys. Rev. A **61**, 040301 (2000), arXiv:quant-ph/9911117.

[6] Barbara M. Terhal, *Bell inequalities and the separability criterion,* Phys. Lett. A **271**, 319 (2000), arXiv:quant-ph/9911057.

[7] Michał Horodecki, Paweł Horodecki, and Ryszard Horodecki, *Separability of mixed states: necessary and sufficient conditions,* Phys. Lett. A **223**, 1 (1996), arXiv:quant-ph/9605038.

[8] Allen Scheie, Pontus Laurell, Anjana M. Samarakoon, Bella Lake, Stephen Nagler, Garrett Granroth, Satoshi Okamoto, Geraldine Alvarez, and Alan Tennant, *Witnessing entanglement in quantum magnets using neutron scattering,* Phys. Rev. B **103**, 224434 (2021), arXiv:2102.08376.

[9] Allen Scheie, Esteban A. Ghioldi, Jie Xing, Joseph A. M. Paddison, Nicholas E. Sherman, Maxime Dupont, Liurukara D. Sanjeewa, Sangyun Lee, Andrew J. Woods, Douglas Abernathy, Daniel M. Pajerowski, Travis J. Williams, Shang-Shun Zhang, Luis O. Manuel, Adolfo E. Trumper, Chaitanya D. Pemmaraju, Athena S. Sefat, David S. Parker, Tom P. Devereaux, Roman Movshovich, Joel E. Moore, Cristian D.

Batista, and Alan Tennant, *Witnessing quantum criticality and entanglement in the triangular antiferromagnet $KYbSe_2$,* arXiv:2109.11527 [cond-mat.str-el] (2023).

[10] George Mathew, Saulo L. L. Silva, Anil Jain, Arya Mohan, Devashibhai T. Adroja, Victoria G. Sakai, C. V. Tomy, Alok Banerjee, Rajendar Goreti, Aswathi V. N., Ranjit Singh, and Deepshikha Jaiswal-Nagar, *Experimental realization of multipartite entanglement via quantum Fisher information in a uniform antiferromagnetic quantum spin chain,* Phys. Rev. Res. **2**, 043329 (2020), arXiv:2010.15747.

[11] Valerie Coffman, Joydip Kundu, and William K. Wootters, *Distributed entanglement,* Phys. Rev. A **61**, 052306 (2000), arXiv:quant-ph/9907047.

[12] Luigi Amico, Andreas Osterloh, Francesco Plastina, Rosario Fazio, and G. Massimo Palma, *Dynamics of entanglement in one-dimensional spin systems,* Phys. Rev. A **69**, 022304 (2004), arXiv:quant-ph/0307048.

[13] Scott Hill and William K. Wootters, *Entanglement of a Pair of Quantum Bits,* Phys. Rev. Lett. **78**, 5022 (1997), arXiv:quant-ph/9703041.

[14] Ryszard Horodecki, Paweł Horodecki, Michał Horodecki, and Karol Horodecki, *Quantum entanglement,* Rev. Mod. Phys. **81**, 865 (2009), arXiv:quant-ph/0702225.

[15] Pranaw Rungta, Vladimír Bužek, Carlton M. Caves, Mark Hillery, and Gerard J. Milburn, *Universal state inversion and concurrence in arbitrary dimensions,* Phys. Rev. A **64**, 042315 (2001), arXiv:quant-ph/0102040.

[16] Vineeth S. Bhaskara and Prasanta K. Panigrahi, *Generalized concurrence measure for faithful quantification of multiparticle pure state entanglement using Lagrange's identity and wedge product,* Quantum Inf. Process. **16**, 1568 (2017), arXiv:1607.00164.

[17] S. Nibedita Swain, Vineeth S. Bhaskara, and Prasanta K. Panigrahi, *Generalized entanglement measure for continuous-variable systems,* Phys. Rev. A **105**, 052441 (2022), arXiv:1706.01448.

[18] Zhi-Hao Ma, Zhi-Hua Chen, Jing-Ling Chen, Christoph Spengler, Andreas Gabriel, and Marcus Huber, *Measure of genuine multipartite entanglement with computable lower bounds,* Phys. Rev. A **83**, 062325 (2011), arXiv:1101.2001.

[19] Allen Scheie, Pontus Laurell, Elbio Dagotto, D. Alan Tennant, and Tommaso Roscilde, *Reconstructing the spatial structure of quantum correlations,* arXiv:2306.11723 [cond-mat.str-el] (2023).

[20] Nicolas Laflorencie, *Quantum entanglement in condensed matter systems,* Phys. Rep. **646**, 1 (2016), arXiv:1512.03388.

[21] Mechthild Enderle, *Neutrons and magnetism,* JDN **13**, 01002 (2014).

[22] Andrew T. Boothroyd, *Principles of Neutron Scattering from Condensed matter* (Oxford University Press, 2020).

[23] Jean-Xavier Boucherle and J. Schweizer, *Magnetic form factor in anomalous intermetallic Ce compounds,* Physica B+C **130**, 337 (1985).

[24] Igor A. Zaliznyak and John M. Tranquada, *Neutron Scattering and Its Application to Strongly Correlated Systems,* in *Springer Ser. Solid-State Sci.* (Springer Berlin Heidelberg, 2014) pp. 205–235, arXiv:1304.4214.

[25] Oliver Marty, Michael Epping, Hermann Kampermann, Dagmar Bruß, Martin B. Plenio, and Marcus Cramer, *Quantifying entanglement with scattering experiments,* Phys. Rev. B **89**, 125117 (2014), arXiv:1310.0929.

[26] Otfried Gühne and Géza Tóth, *Entanglement detection,* Phys. Rep. **474**, 1 (2009), arXiv:quant-ph/0811.2803.

[27] Géza Tóth, *Entanglement witnesses in spin models,* Phys. Rev. A **71**, 010301 (2005), arXiv:quant-ph/0406061.

[28] Otfried Gühne, Géza Tóth, and Hans J Briegel, *Multipartite entanglement in spin chains,* New J. Phys. **7**, 229 (2005), arXiv:quant-ph/0502160.

[29] Otfried Gühne and Géza Tóth, *Energy and multipartite entanglement in multidimensional and frustrated spin models,* Phys. Rev. A **73**, 052319 (2006), arXiv:quant-ph/0510186.

[30] Marcin Wieśniak, Vlatko Vedral, and Časlav Brukner, *Magnetic susceptibility as a macroscopic entanglement witness,* New J. Phys. **7**, 258 (2005), arXiv:quant-ph/0503037.

[31] Časlav Brukner, Vlatko Vedral, and Anton Zeilinger, *Crucial role of quantum entanglement in bulk properties of solids,* Phys. Rev. A **73**, 012110 (2006), arXiv:quant-ph/0410138.

[32] Philipp Krammer, Hermann Kampermann, Dagmar Bruß, Reinhold A. Bertlmann, Leong Chuang Kwek, and Chiara Macchiavello, *Multipartite Entanglement Detection via Structure Factors,* Phys. Rev. Lett. **103**, 100502 (2009), arXiv:0904.3860.

[33] Carl W. Helstrom, *Quantum detection and estimation theory* (Academic Press New York, 1976) p. 309.

[34] Alexander S. Holevo, *Probabilistic and Statistical Aspects of Quantum Theory* (Probabilistic and Statistical Aspects of Quantum Theory, 2011).

[35] Samuel L. Braunstein and Carlton M. Caves, *Statistical distance and the geometry of quantum states,* Phys. Rev. Lett. **72**, 3439 (1994).

[36] Géza Tóth, Christian Knapp, Otfried Gühne, and Hans J. Briegel, *Spin squeezing and entanglement,* Phys. Rev. A **79**, 042334 (2009), arXiv:0806.1048.

[37] Giuseppe Vitagliano, Philipp Hyllus, Iñigo L. Egusquiza, and Géza Tóth, *Spin Squeezing Inequalities for Arbitrary Spin,* Phys. Rev. Lett. **107**, 240502 (2011), arXiv:1104.3147.

[38] Giuseppe Vitagliano, Iagoba Apellaniz, Iñigo L. Egusquiza, and Géza Tóth, *Spin squeezing and entanglement for an arbitrary spin,* Phys. Rev. A **89**, 032307 (2014).

[39] Géza Tóth, Christian Knapp, Otfried Gühne, and Hans J. Briegel, *Optimal Spin Squeezing Inequalities Detect Bound Entanglement in Spin Models,* Phys. Rev. Lett. **99**, 250405 (2007), arXiv:quant-ph/0702219.

[40] Manuel Gessner, Luca Pezzé, and Augusto Smerzi, *Efficient entanglement criteria for discrete, continuous, and hybrid variables,* Phys. Rev. A **94**, 020101 (2016), arXiv:1608.02421.

[41] Luca Pezzé and Augusto Smerzi, *Entanglement, Nonlinear Dynamics, and the Heisenberg Limit,* Phys. Rev. Lett. **102**, 100401 (2009), arXiv:0711.4840.

[42] Florian Fröwis and Wolfgang Dür, *Measures of macroscopicity for quantum spin systems,* New J. Phys. **14**, 093039 (2012), arXiv:1205.3048.

[43] Géza Tóth, *Entanglement detection and quantum metrology in quantum optical systems,* Budapest: Doctoral Dissertation submitted to the Hungarian Academy of Sciences (2021).

[44] Philipp Hauke, Markus Heyl, Luca Tagliacozzo, and Peter Zoller, *Measuring multipartite entanglement through dynamic susceptibilities,* Nat. Phys. **12**, 778 (2016), arXiv:1509.01739.

[45] Giuseppe Vitagliano, Giorgio Colangelo, Ferran Martin Ciurana, Morgan W. Mitchell, Robert J. Sewell, and Géza Tóth, *Entanglement and extreme planar spin squeezing,* Phys. Rev. A **97**, 020301 (2018), arXiv:1705.09090.

[46] Anders S. Sørensen and Klaus Mølmer, *Entanglement and extreme spin squeezing,* Phys. Rev. Lett. **86**, 4431 (2001), arXiv:quant-ph/0011035.

[47] Oliver Marty, Marcus Cramer, Giuseppe Vitagliano, Géza Tóth, and Martin B. Plenio, *Multiparticle entanglement criteria for nonsymmetric collective variances,* arXiv:1708.06986 [quant-ph] (2017).

[48] Giuseppe Vitagliano, Iagoba Apellaniz, Matthias Kleinmann, Bernd Lücke, Carsten Klempt, and Géza Tóth, *Entanglement and extreme spin squeezing of unpolarized states,* New J. Phys. **19**, 013027 (2017), arXiv:1605.07202.

[49] Guangyong Xu, Zhijun Xu, and J. M. Tranquada, *Absolute cross-section normalization of magnetic neutron scattering data,* Rev. Sci. Instrum. **84**, 083906 (2013), arXiv:1305.5521.

[50] Valentina Martelli, Ang Cai, Emilian M. Nica, Mathieu Taupin, Andrey Prokofiev, Chia-Chuan Liu, Hsin-Hua Lai, Rong Yu, Kevin Ingersent, Robert Küchler, André M. Strydom, Diana Geiger, Jonathan Haenel, Julio Larrea, Qimiao Si, and Silke Paschen, *Sequential localization of a complex electron fluid,* PNAS **116**, 17701 (2019), arXiv:1709.09376.

[51] Christian Franz, Steffen Säubert, Andreas Wendl, Franz X. Haslbeck, Olaf Soltwedel, Johanna K. Jochum, Leonie Spitz, Jonas Kindervater, Andreas Bauer, Peter Böni, and Christian Pfleiderer, *MIEZE Neutron Spin-Echo Spectroscopy of Strongly Correlated Electron Systems,* JPSJ **88**, 081002 (2019), arXiv:2104.01389.

[52] Abu Ashik Md Irfan, Patrick Blackstone, Roger Pynn, and Gerardo Ortiz, *Quantum entangled-probe scattering theory,* New J. Phys. **23**, 083022 (2021), arXiv:2008.04328.

[53] Nikolai A Sinitsyn and Yuriy V Pershin, *The Theory of Spin Noise Spectroscopy: A Review,* Rep. Prog. Phys. **79**, 106501 (2016), arXiv:1603.06858.

[54] Bimla Danu, Matthias Vojta, Fakher F. Assaad, and Tarun Grover, *Kondo Breakdown in a Spin-1/2-Chain of Adatoms on a Dirac Semimetal,* Phys. Rev. Lett. **125**, 206602 (2020), arXiv:2005.10278.

[55] Sean Vig, Anshul Kogar, Matteo Mitrano, Ali Husain, Luc Venema, Mindy Rak, Vivek Mishra, Peter Johnson, Genda Gu, Eduardo Fradkin, Michael Norman, and Peter Abbamonte, *Measurement of the dynamic charge response of materials using low-energy, momentum-resolved electron energy-loss spectroscopy (M-EELS),* SciPost Phys. **3**, 026 (2017), arXiv:1509.04230